Geochimica et Cosmochimica Acta 344 (2023) 207–229

Contents lists available at ScienceDirect

Geochimica et Cosmochimica Acta

journal homepage: www.elsevier.com/locate/gca

Rubidium and potassium isotopic variations in chondrites and Mars: Accretion signatures and planetary overprints

Nicole X. Nie [a,b,*], Xin-Yang Chen [c,d], Zhe J. Zhang [a], Justin Y. Hu [a,e], Weiyi Liu [b], Francois L.H. Tissot [b], Fang-Zhen Teng [c], Anat Shahar [f], Nicolas Dauphas [a]

[a] Origins Laboratory, Department of the Geophysical Sciences and Enrico Fermi Institute, The University of Chicago, Chicago, IL 60637, USA
[b] The Isotoparium, Division of Geological and Planetary Sciences, California Institute of Technology, Pasadena, CA 91125, USA
[c] Isotope Laboratory, Department of Earth and Space Sciences, University of Washington, Seattle, WA 98195, USA
[d] Institute of Sedimentary Geology, Chengdu University of Technology, Chengdu, China
[e] Department of Earth Sciences, University of Cambridge, Downing Street, Cambridge CB2 3EQ, UK
[f] Earth and Planets Laboratory, Carnegie Institution for Science, Washington, DC 20015, USA

ARTICLE INFO

Article history:
Received 16 August 2022
Accepted 4 January 2023
Available online 7 January 2023
Associate editor: Shichun Huang

Keywords:
Rb isotopes
K isotopes
Ordinary chondrites
Enstatite chondrites
Isotope fractionation of moderately volatile elements

ABSTRACT

As moderately volatile elements, isotopes of Rb and K can trace volatilization processes in planetary bodies. Rubidium isotopic data are however very scarce, especially for non-carbonaceous meteorites. Here, we report combined Rb and K isotopic data ($\delta^{87/85}$Rb and $\delta^{41/39}$K) for 7 ordinary, 6 enstatite, and 4 Martian meteorite falls to understand the causes for the variations in volatile abundances and isotopic compositions. Bulk Rb and K isotopic compositions of planetary bodies are estimated to be (Table 1): Mars +0.10 ± 0.03 ‰ for Rb and −0.26 ± 0.05 ‰ for K, bulk OCs $-0.12^{+0.15}_{-0.24}$ ‰ for Rb and $-0.72^{+0.28}_{-0.41}$ ‰ for K, bulk ECs $+0.02^{+0.29}_{-0.26}$ ‰ for Rb and $-0.33^{+0.37}_{-0.23}$ ‰ for K. The bulk K isotopic compositions of subgroup OCs are estimated to be $-0.72^{+0.26}_{-0.55}$ ‰ for H chondrites, $-0.71^{+0.23}_{-0.39}$ ‰ for L chondrites, and $-0.77^{+0.63}_{-0.30}$ ‰ for LL chondrites. A broad correlation between the Rb and K isotopic compositions of planetary bodies is observed. The correlation follows a slope that is consistent with kinetic evaporation and condensation processes, suggesting volatility-controlled mass-dependent isotope fractionation (as opposed to nucleosynthetic anomalies).

Individual ordinary and enstatite chondrites show large Rb and K isotopic variations (−1.02 to +0.29 ‰ for Rb and −0.91 to −0.15 ‰ for K). Samples of lower metamorphic grades display correlated elemental and isotopic fractionations between Rb and K, while samples of higher metamorphic grades show great scatter, suggesting that chondrite parent-body processes have decoupled the two elements and their isotopes at the sample scale. Several processes could have contributed to the observed isotopic variations of Rb and K, including (i) chondrule "nugget effect", (ii) volatilization during parent-body thermal metamorphism (heat-induced vaporization and gas transport within parent bodies), (iii) thermal diffusion during parent-body metamorphism, and (iv) impact/shock heating. Quantitative modeling of the first two processes suggests that neither of them could produce isotopic variations large enough to explain the observed isotopic variations. Volatilization during parent-body thermal metamorphism [the scenario (ii)], which has been commonly invoked to explain the isotopic variations of volatile elements, is gas transport-limited and its effect on isotopic fractionations of moderately volatile elements should be negligible. Modeling of diffusion processes suggests that (iii) could produce K isotopic variation comparable to the observed variation. The large isotopic variations in non-carbonaceous meteorites are thus most likely due to diffusive redistribution of K and Rb during metamorphism and/or shock-induced heating and vaporization.

1. Introduction

Rubidium (Rb) and potassium (K) are two common alkali metal elements (other alkali metal elements are Li, Na, Cs, and unstable Fr) with similar geochemical behaviors. They are highly concen-

* Corresponding author at: Origins Laboratory, Department of the Geophysical Sciences and Enrico Fermi Institute, The University of Chicago, Chicago, IL 60637, USA.
E-mail address: nxnie@caltech.edu (N.X. Nie).

https://doi.org/10.1016/j.gca.2023.01.004
0016-7037/

trated in the continental crust (Wedepohl, 1995; Rudnick and Gao, 2003) because of their lithophile and highly incompatible nature. Many studies have documented K and to a lesser extent Rb isotopic variations in rocks and fluids, and the observed K and Rb isotopic variations in natural samples are about ±1.5 ‰ for K and ±1 ‰ for Rb (e.g., Alexander et al., 2000; Alexander and Grossman, 2005; Hille et al., 2019; Hu et al., 2020; Huang et al., 2020; Humayun and Clayton, 1995a, 1995b; Humayun and Koeberl, 2004; Koefoed et al., 2020; Li et al., 2019a, 2021a, Liu et al., 2020, 2021b; Nebel et al., 2011; Nie and Dauphas, 2019; Parendo et al., 2017; Pringle and Moynier, 2017; Ramos et al., 2018; Taylor et al., 2005; Tuller-Ross et al., 2019; Wang and Jacobsen, 2016a, 2016b; Xu et al., 2019; Sun et al., 2020; Zhao et al., 2020; Bloom et al., 2020; Ku and Jacobsen, 2020; Jiang et al., 2021; Wang et al., 2021a; Magna et al., 2021; Nie et al., 2021b, a; Hu et al., 2021c; Wang et al., 2021b; Tian et al., 2021, 2022; Wang et al., 2022). Many of those isotopic analyses were done in the past couple of years, due in part to improvements in the chemical purification and MC-ICPMS measurement techniques (Chen et al., 2019, 2021, Hu et al., 2018, 2021a; Li et al., 2022; Morgan et al., 2018; Moynier et al., 2021; Nie et al., 2021c; Nie and Dauphas, 2019; Wang and Jacobsen, 2016a; Zhang et al., 2018). Because they are highly fluid mobile and moderately volatile, Rb and K isotopes have been used to trace terrestrial weathering, sea floor alteration, and volatilization accompanying the formation and accretion of planetary bodies in the early solar system (e.g., Alexander et al., 2000; Alexander and Grossman, 2005; Bloom et al., 2020; Hu et al., 2020, 2021c; Humayun and Clayton, 1995a; Koefoed et al., 2020; Li et al., 2019a, 2021b; Liu et al., 2021a; Nebel et al., 2011; Nie et al., 2021a, 2021b; Nie and Dauphas, 2019; Parendo et al., 2017; Pringle and Moynier, 2017; Ramos et al., 2018; Sun et al., 2020; Tian et al., 2021, 2022, Wang et al., 2021b, 2022; Wang and Jacobsen, 2016a; Zhao et al., 2020).

In cosmochemistry, an outstanding question that remains unsettled is why planetary bodies are depleted in moderately volatile elements (MVEs) compared to solar composition (represented by CI chondrites). The depletion is often quantified by Rb/Sr and K/U ratios (e.g., Halliday and Porcelli, 2001; Davis, 2006; Dauphas et al., 2022). Studying volatile depletion processes could help us better understand the nebular and planetary processes that shaped the Solar System. Rubidium and potassium make a perfect pair for tracing volatile depletion processes because,

(i) Rb and K are both highly lithophile, incompatible, and monovalent (Heier and Adams, 1964). These characteristics simplify interpretations because planetary processes such as core formation, partial melting, and fractional crystallization are unlikely to fractionate isotopically those two elements or decouple them from refractory lithophile incompatible elements such as Th, U, Ba, and La.

(ii) While Rb and K have similar geochemical behaviors, they have different volatilities (the 50 % condensation temperatures of Rb and K under solar nebula conditions are ~ 800 and 1000 K, respectively; Lodders, 2003; Wood et al., 2019) and different masses, so they provide complementary pieces of information on the processes (evaporation, condensation, hydrodynamic escape) and conditions (temperature, vapor saturation) of MVE loss in the nebula and planetary bodies.

Several studies have already demonstrated the virtue of combining Rb and K isotopic analyses on the same samples. Nie and Dauphas (2019) used Rb and K isotopic compositions of lunar samples to show that lunar volatile depletion relative to the Earth was due to partial evaporation of volatile elements in a medium that was ~ 99 % saturated for most MVEs, possibly consistent with viscous drainage of MVEs from the protolunar disk onto the proto-Earth. Nie et al. (2021a) reported correlated isotopic variations for K, Rb, and other MVEs in carbonaceous chondrites (CCs), demonstrating that kinetic isotope fractionation associated with volatile condensation in chondrule melt, followed by chondrule-matrix mixing, was responsible for K isotopic variations in CCs, rather than nucleosynthetic anomalies as had been suggested previously (Ku and Jacobsen, 2020). Nie et al. (2021a) focused on CCs because previous studies had suggested that the isotopic compositions of CCs could be described as a two-component mixture between chondrules and matrix (e.g., Alexander, 2019; Hellmann et al., 2020), and the study confirmed this interpretation. While non-carbonaceous chondrites (NCs) have been measured for their K isotopic compositions (Bloom et al., 2020; Zhao et al., 2020; Ku and Jacobsen, 2020), the causes for the K isotopic variations remain elusive and no coupled Rb isotopic data have been reported. The only Rb isotopic data available for an NC was measured in Krymka (LL3.2) (Pringle and Moynier, 2017). In this study, we performed combined Rb and K isotopic analyses of enstatite chondrites (ECs), ordinary chondrites (OCs), and Martian meteorites, to shed new light on the processes responsible for K and Rb isotopic variations. We also aim to constrain and compare the bulk Rb and K isotopic compositions of planetary bodies. We show that the Rb and K isotopic compositions of bulk planetary bodies display a broad correlation that reflects planetary scale evaporation/condensation processes. In addition, the Rb and K isotopic compositions vary largely among individual NC samples, suggesting that the isotopic compositions have been overprinted by parent-body processes (owing to the fluid mobile and thermally labile nature of the two elements).

2. Samples and methods

2.1. Samples

All the selected meteorite samples but one (Atlanta) are observed meteorite falls. The reason for avoiding finds is that K and Rb are highly fluid mobile and could easily be weathered or contaminated on terrestrial surface. Indeed, the upper continental crust is enriched in K and Rb compared to meteorites, by a factor of ~ 30 [~3 wt% K and 84 ppm Rb in the upper continental crust (Rudnick and Gao, 2003), compared to OCs and ECs, in which K and Rb abundances are ~ 780 ppm and 3 ppm, respectively]. The meteorite find Atlanta was measured to assess the possible effect of terrestrial weathering/contamination.

Correlated Rb and K isotopic compositions have been reported for carbonaceous chondrites (Nie et al., 2021a), but not for other types of meteorites. Here we measure the isotopic compositions of the two elements in the same samples, including 7 OCs (Kesen H4, Queen's Mercy H6, Bald Mountain L4, Farmington L5, Krymka LL3.2, Soko-Banja LL4, and Saint-Séverin LL6), 6 ECs (Abee EH4, Indarch EH4, Saint-Sauveur EH5, Hvittis EL6, Pillistfer EL6, and Atlanta EL6), and 4 Martian meteorites (Shergotty, Zagami, Chassigny, and Nakhla) (Table 1). The chondrites comprise meteorite subgroups H, L, LL, EH, and EL, with petrologic type ranging from 3 to 6, where samples of petrologic type 3 are the most primitive while those of type 6 have experienced extensive thermal metamorphism and associated recrystallization and equilibration.

We also report the K isotopic compositions of 6 lunar basaltic samples (12002–613, 12018–301,12052–353, 74275–361, 10017–413, and 77215–276) that were analyzed previously for their Rb isotopic compositions (Nie and Dauphas, 2019). The K isotopic compositions were measured on the exact same sample aliquots as were already measured for Rb.

2.2. Analytical methods

Sample digestion. The procedure of sample digestion follows previously established method (Nie and Dauphas, 2019; Nie

Table 1
Rubidium and potassium isotopic compositions.

Sample	Type	Fall/Find	Diss. mass (mg)	$\delta^{87/85}$Rb (‰)	95 % c.i.	n_{Rb}	$\delta^{41/39}$K (‰)	95 % c.i.	n_K	K (ug/g)	Rb (ug/g)
Carbonaceous chondrites											
Orgueil	CI1	Fall	91.3[a]	0.194[a]	0.034[a]	9	−0.039[a]	0.046[a]	7	390.9[a]	1.9[a]
Orgueil	CI1	Fall	101.6[a]	0.159[a]	0.042[a]	8	−0.144[a]	0.082[a]	5	490.6[a]	2.1[a]
Ivuna	CI1	Fall	99.6[a]	0.131[a]	0.042[a]	8	−0.460[a]	0.059[a]	6	457.5[a]	1.8[a]
Murchison	CM2	Fall	90.7[a]	0.119[a]	0.024[a]	11	−0.101[a]	0.042[a]	7	320.2[a]	1.5[a]
Mighei	CM2	Fall	91.5[a]	0.126[a]	0.032[a]	10	−0.158[a]	0.059[a]	6	394.3[a]	1.5[a]
Allende	CV3	Fall	118.9[a]	0.091[a]	0.024[a]	11	−0.201[a]	0.046[a]	7	256.2[a]	1.1[a]
Vigarano	CV3	Fall	97.0[a]	0.057[a]	0.020[a]	8	−0.346[a]	0.046[a]	7	269.8[a]	1.0[a]
Ornans	CO3.4	Fall	99.4[a]	0.100[a]	0.024[a]	11	−0.046[a]	0.046[a]	7	344.7[a]	1.3[a]
Lancé	CO3.5	Fall	107.0[a]	0.029[a]	0.030[a]	10	−0.235[a]	0.042[a]	7	346.0[a]	1.0[a]
Ordinary chondrites											
Kesen	H4	Fall	100.3	−1.024	0.026	9	−0.617	0.042	7	664.4	2.3
Queen's Mercy	H6	Fall	112.8	0.045	0.034	12	−0.461	0.045	7	939.4	2.6
Bald Mountain	L4	Fall	114.4	−0.512	0.034	12	−0.912	0.045	7	762.3	2.6
Farmington	L5	Fall	143.9	0.146	0.021	10	−0.484	0.040	7	851.7	1.8
Farmington	L5	Fall	100.4	0.207	0.034	9	−0.486	0.074	7	753.5	1.6
Krymka	LL3.2	Fall	100.7	−0.407	0.040	9	−0.754	0.051	6	907.9	3.3
Soko-banja	LL4	Fall	106.8	−0.821	0.030	15	−0.468	0.045	7	551.8	1.6
Saint-Séverin	LL6	Fall	120.9	0.180	0.034	7	−0.152	0.040	7	874.2	0.6
Enstatite chondrites											
Abee	EH4	Fall	126.8	−0.242	0.021	10	−0.293	0.040	7	1058.5	4.8
Abee	EH4	Fall	111.3	−0.193	0.019	8	−0.280	0.084	6	984.5	4.3
Indarch	EH4	Fall	136.8	−0.096	0.021	10	−0.366	0.040	7	842.3	3.3
Indarch	EH4	Fall	102.2	−0.035	0.020	7	−0.325	0.048	6	772.5	3.2
Indarch	EH4	Fall	100.6	−0.079	0.031	9	−0.310	0.048	6	721.0	3.3
Saint-Sauveur	EH5	Fall	99.3	0.045	0.036	12	−0.295	0.048	6	712.2	3.0
Hvittis	EL6	Fall	110.3	0.294	0.020	10	−0.148	0.048	6	582.9	2.7
Pillistfer	EL6	Fall	99.3	0.150	0.052	10	−0.542	0.042	7	758.4	1.8
Atlanta	EL6	Find	105.1	2.454	0.019	9	−0.162	0.040	7	635.5	1.2
Martian meteorites											
Shergotty	Shergottite	Fall	44.6	0.055	0.021	9	−0.356	0.042	7	1472.9	7.0
Zagami	Shergottite	Fall	48.0	0.052	0.025	10	−0.075	0.042	7	971.0	4.8
Chassigny	Chassignite	Fall	94.0	0.111	0.063	5	−0.285	0.042	7	198.0	0.5
Nakhla	Nakhlite	Fall	52.1	0.138	0.063	5	−0.216	0.042	7	844.4	3.3
Lunar rocks											
12002.613	Olivine basalt		100.1	−0.034[b]	0.036[b]	9	−0.033	0.059	6	431.0	0.9
12018.301	Olivine basalt		100.2	0.011[b]	0.043[b]	8	−0.027	0.052	7	398.5	0.9
12052.353	Pigeonite basalt		101.3	−0.003[b]	0.036[b]	9	−0.024	0.052	7	516.9	1.1
74275.361	Ilmenite basalt		100.8	0.089[b]	0.058[b]	7	−0.029	0.052	7	644.0	0.9
10017.413	Ilmenite basalt		50.5	0.060[b]	0.029[b]	9	0.052	0.052	7	2476.3	5.3
77215.276	Cataclastic norite		51.3	−0.149[b]	0.032[b]	10	−0.002	0.052	7	1187.4	3.3
Terrestrial geostandards											
BCR-2	Basalt			−0.155[c]	0.005[c]		−0.423[a]	0.037[a]			
BHVO-2	Basalt			−0.114[c]	0.006[c]		−0.391[a]	0.078[a]			
BE-N	Basalt			−0.103[c]	0.018[c]		−0.396	0.046			
W-2	Diabase			−0.147[c]	0.014[c]		−0.383	0.069			
AGV-2	Andesite			−0.146[c]	0.012[c]		−0.462[a]	0.044[a]			
GSR-1	Granite			−0.178[c]	0.019[c]		−0.527	0.045			
GS-N	Granite			−0.177[c]	0.014[c]		−0.441	0.062			
G-A	Granite			−0.234[c]	0.020[c]		−0.435	0.042			
G-3	Granite			−0.234[c]	0.009[c]		−0.439[a]	0.033[a]			
Bulk planetary compositions											
Bulk CI				0.17[a]	0.02[a]		−0.07[a]	0.61[a]			
Bulk CM				0.12[a]	0.02[a]		−0.12[a]	0.35[a]			
Bulk CV				0.07[a]	0.21[a]		−0.27[a]	0.92[a]			
Bulk CO				0.07[a]	0.44[a]		−0.15[a]	1.19[a]			
Bulk OC				−0.12	+0.15/-0.24		−0.72	+0.28/-0.41			
H							−0.72	+0.26/-0.55			
L							−0.71	+0.23/-0.39			
LL							−0.77	+0.63/-0.30			
Bulk EC				0.02	+0.29/-0.26		−0.33	+0.37/-0.23			
Bulk Mars				0.10	0.03		−0.26	0.05			
Bulk Earth				−0.13[b]	0.01[b]		−0.44	0.02			
Bulk Moon				0.03[b]	0.03[b]		−0.01	0.02			

Rubidium isotopic compositions are relative to the reference standard SRM984. Potassium isotopic compositions are relative to the reference standard SRM3141a. a. Data from Nie et al. (2021a). b. Data from Nie and Dauphas (2019). c. Data from Nie and Dauphas (2019) and Nie et al. (2021a, c). n_{Rb} and n_K are the numbers of duplicate analysis of Rb and K for each sample.

et al., 2021c) and is briefly described here. Sample powders of bulk meteorites, weighing from 50 to 120 mg (from bulk homogenized powders with masses of more than 200 mg), were transferred to 30 mL Savillex PFA vials. The powders were first treated with 2:1 volume mixture of concentrated HF-HNO_3 with a few drops of $HClO_4$ at 130 °C for 24–48 h. The solutions were then dried down, taken up in aqua regia (3:1 volume mixture of concentrated HCl and HNO_3), and heated at 130 °C for 24 h. The aqua regia step was repeated another time, followed by dry-down and re-dissolution of the samples in concentrated HNO_3. Clear sample solutions at this stage were ready for column chemistry. Chondritic samples are, however, difficult to digest because they contain acid-resistant pre-solar phases. For these samples, an extra step of bomb digestion was performed on the residues after removal of the clear supernatant solution. The residues were transferred to 5 mL Savillex PFA vials filled with 3:1 volume mixture of concentrated HF-HNO_3. The vials were then placed in Parr bombs, heated to 180 °C for at least 3 days. The bombed solutions were then combined with the supernatant solutions. The bomb step ensured complete digestion of the samples. The sample solutions were then evaporated and re-dissolved in 1 M HNO_3 for ion-exchange column chromatography.

Potassium and rubidium column chromatography. Because the K/Rb ratio in natural samples is high (200 to 1500 g/g; Dauphas et al., 2022), all studies focused on K isotopic analysis do not separate Rb from K as there is no direct isobaric interference on K from Rb and no associated matrix effect. Rubidium isotopic analysis however requires separation of Rb from K to avoid matrix-induced instrumental fractionation. The two elements have very similar partition behaviors on most resins and are difficult to separate cleanly and quantitatively from each other. After evaluation of several purification protocols based on AMP-PAN resin, cation exchange resin, and Sr-Spec resin, a K-Rb purification method was developed to separate K and Rb cleanly from the same digested solutions (Nie et al., 2021c). It involves four steps of column chromatography. Sample solutions (in 1 M HNO_3) are first loaded onto Bio-Rad Econo-Pac columns, each packed with 16 mL AG50W-X8 resin (200–400 mesh), and 160 mL 1 M HNO_3 is run through each column to collect Rb and K, together with several other elements. During the elution, matrix elements such as Mg, Fe, and Ca remain on the resin while K and Rb are eluted together. After drying down and redissolution in 0.5 M HNO_3, the solutions are loaded onto the same resin columns (after cleaning each column with 240 mL 6 M HNO_3) for a finer separation. Matrix elements are eluted first with 130 mL of 0.5 M HNO_3, and Rb and K are then quantitatively eluted with 350 mL of 0.5 M HNO_3. The recovered K-Rb fraction is further purified by removing Ti using a 1 mL column of AG1-X8 (200–400 mesh) anion exchange resin. Rubidium and potassium are eluted directly from the column with 9 mL 2 M HF while Ti is bound to the resin. At this stage, the K-Rb solutions should be clean and contain only negligible amounts of other elements. The solutions are then evaporated to dryness and dissolved in 3 M HNO_3 for the last chromatography step. This last step is accomplished using Savillex PFA microcolumns of 0.45 cm internal diameter and 40 cm length, filled with Eichrom crown ether extractant Sr resin of 50–100 μm size. Sample solutions are loaded onto the Sr resin columns in 0.1 mL 3 M HNO_3, then 3.9 mL 3 M HNO_3 is used to elute matrix elements, followed by another 12 mL 3 M HNO_3 to collect Rb and another 20 mL 3 M HNO_3 to collect K. The Sr resin step also helps eliminating any Sr remaining from the previous steps, and this is important because $^{87}Sr^+$ can interfere with $^{87}Rb^+$ signal during mass spectrometry. The partition coefficients of both Rb and K on the Sr resin are low (<10; Horwitz et al., 1992), and we found that some K could be eluted together with Rb when large amount of K was loaded on the column. The quantities of Rb and K in each collected fraction of the Sr column (matrix, Rb, and K fractions) were measured to ensure that K and Rb were quantitatively recovered and completely separated from each other. On some occasions, we found that K and Rb had not been well separated after the Sr resin column, then we passed the impure fraction on the Sr column a second time to isolate Rb and K, after which the isolated Rb and K fractions were recombined as needed. The final purified Rb and K solutions were dried down and re-dissolved in 2 % HNO_3 for isotopic analysis. The Rb and K yields of the overall procedure are greater than 95 %. The procedural blanks for Rb and K were < 0.2 ng and < 20 ng, respectively, and are negligible compared to the quantities of Rb (≥80 ng) and K (≥5 μg) extracted from each sample.

MC-ICPMS measurements. The Rb isotopic measurements were done using a ThermoScientific Neptune Plus MC-ICPMS at the Origins Lab of the University of Chicago following the protocol described previously (Nie and Dauphas, 2019; Nie et al., 2021c). Rubidium solutions were introduced into the torch using a ~ 100 μL/min PFA nebulizer and dual Scott-cyclonic quartz spray chamber (Stable Introduction System). Standard nickel sampler and H skimmer cones and a low-resolution slit were used. Solutions were measured at concentrations of ~ 15–25 ng/g in 2 % HNO_3, yielding an $^{87}Rb^+$ signal of ~ 1–1.5 V. The $^{87}Sr^+$ interference on $^{87}Rb^+$ was corrected for by monitoring $^{88}Sr^+$, and assuming an $^{87}Sr^+/^{88}Sr^+$ ratio of 0.085. Each sample analysis consisted of a single block of 25 cycles of 4.194-s integration time. Instrumental fractionation was corrected for by conventional standard-sample bracketing method. Acid blanks were measured before and after each analysis of standards or samples, and the average was taken and subtracted from the signal intensity of the standard or sample (on peak zero). Each purified sample solution was analyzed 7–15 times and the average value was taken as the isotopic composition of the sample. The uncertainty of the sample was calculated as the 95 % c.i. using the formula of $2\sigma/\sqrt{n}$, where n is the number of replicate analysis of the sample and σ is the standard deviation of the standards bracketed by itself during each analytical session. The σ of the standards (rather than the σ of a sample) was used because the standards were analyzed many more times than each sample during one analytical session and should be a better measure of instrumental stability. Given that the standard is a mono-element reference solution, the uncertainties quantified using it should reflect only the analytical uncertainty associated with MC-ICPMS measurements and do not include the uncertainties induced by sample digestion and chemical purification. Rubidium isotopic compositions were calculated using the conventional δ-notation (Teng et al., 2017) against reference material NIST SRM984,

$$\delta^{87}\mathrm{Rb}(‰) = 1000[(^{87}\mathrm{Rb}/^{85}\mathrm{Rb})_{\mathrm{Sample}}/(^{87}\mathrm{Rb}/^{85}\mathrm{Rb})_{\mathrm{SRM984}} - 1] \quad (1)$$

The $^{41}K/^{39}K$ ratio (^{40}K was not analyzed due to its extremely low abundance and the presence of interferences from ^{40}Ar and possibly ^{40}Ca) was measured on a Nu Plasma II MC-ICPMS at the Isotope Laboratory of the University of Washington, Seattle, following the method described previously (Hu et al., 2018; Xu et al., 2019). The measurements were done using a "cold plasma" method, which involves using a reduced RF forward power of 700 to 1125 W, in contrast with the usual power of 1300 W (Hu et al., 2018). Potassium solutions were introduced into the mass spectrometer using an Aridus II desolvating nebulizer with a flow rate of 100 μL/min, and measured at concentrations of 2–3 μg/g in 2 % HNO_3, yielding a signal intensity of 4.5–6.5 V on ^{39}K. The ArH^+ interferences on isotopes ^{41}K and ^{39}K were partially resolved by using a high-resolution slit, and the signals of the two K isotopes were measured at interference-free peak shoulders. Standard-sample bracketing was used to correct for instrumental fractiona-

tion. Each sample/standard analysis consisted of 50 cycles of 4.194-s integration time. Acid blank was measured at the beginning of each analytical session and was subtracted from the ion intensities of the samples and standards. Like for Rb, each purified sample solution was analyzed 5–7 times, the average was taken, and the uncertainty was calculated as the 95 % c.i.. The K isotopic compositions of samples are reported in δ^{41}K notation, relative to the reference material NIST SRM3141a,

$$\delta^{41}\mathrm{K}(‰) = 1000[(^{41}\mathrm{K}/^{39}\mathrm{K})_{\mathrm{Sample}}/(^{41}\mathrm{K}/^{39}\mathrm{K})_{\mathrm{SRM3141a}} - 1] \quad (2)$$

3. Results

The Rb and K isotopic compositions of OCs, ECs, and Martian meteorites, and the K isotopic compositions of lunar samples measured in this study are reported in Table 1. The previously reported Rb and K isotopic compositions of CCs (Nie et al., 2021a) and the Rb isotopic compositions of the lunar samples (Nie and Dauphas, 2019) are also compiled in Table 1 for reference. All data are plotted in Fig. 1.

Because of the terrestrial surface conditions and the high K and Rb concentrations in the continental crust, meteorites can be prone to terrestrial weathering or contamination during handling (Tian et al., 2019). The most extreme isotopic composition obtained from this study is the Rb isotopic composition of the meteorite find Atlanta (EL6), which has a heavy δ^{87}Rb value of + 2.45 ‰. The Rb concentration in this sample is a factor of 1.5–2.2 lower than the other two EL6 meteorites, indicating that Rb has been mobilized and isotopically fractionated by terrestrial weathering. The K content and isotopic composition in this sample are similar to those of the other two EL6 samples, meaning that K and Rb can be affected differently by terrestrial weathering. Previous work on K isotopes of HED meteorites revealed that hot desert meteorite finds can display significantly higher K concentrations and heavier K isotopic compositions than more pristine samples, suggesting that weathering can modify K isotopic system as well (Tian et al., 2019). To avoid this potential problem, we have focused mainly on meteorite falls that experienced the least alteration.

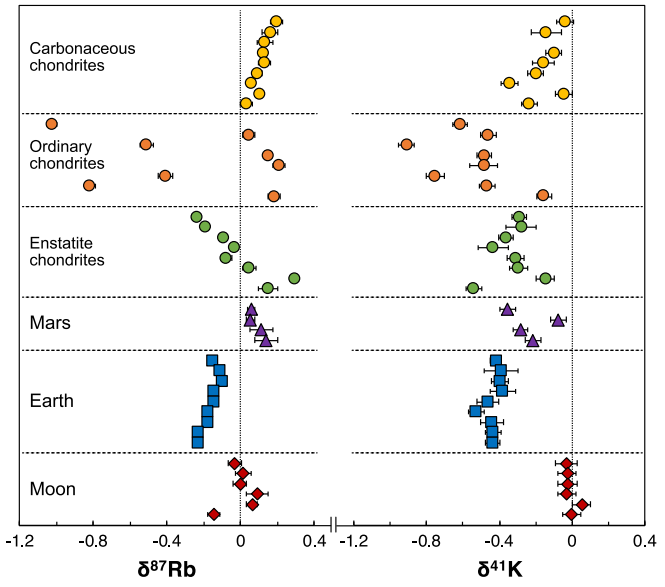

Fig. 1. Rubidium and potassium isotopic compositions of chondrites, Mars, Earth, and Moon (Table 1). Differentiated bodies show relatively small isotopic variations while chondrites show large isotopic variations. In particular, ordinary chondrites show large Rb and K isotopic variations extending to extremely light values. Samples are arranged in the same sequence as they are in Table 1 based on their groups and petrologic types.

Igneous rocks from differentiated planetary bodies such as Earth, Moon, and Mars display limited isotopic variations given analytical uncertainties of ~±0.03 ‰ for δ^{87}Rb and ~±0.05 ‰ for δ^{41}K. Terrestrial igneous rocks define a narrow range of Rb and K isotopic compositions, from −0.24 to −0.11 ‰ for δ^{87}Rb and −0.53 to −0.38 ‰ for δ^{41}K (Table 1 and Fig. 1). Lunar samples (various basalts and a norite) show limited δ^{87}Rb isotopic variation of −0.15 to +0.09 ‰ and δ^{41}K isotopic variation of −0.03 to +0.05 ‰, with most compositions overlapping within error. Unlike isotopic compositions, the elemental concentrations of lunar rocks vary largely, 0.9 to 5.3 μg/g for Rb and 399 to 2476 μg/g for K, suggesting that lunar magma ocean differentiation redistributed elements but did not fractionate much isotopes. The Martian samples have δ^{87}Rb isotopic compositions ranging from +0.05 to +0.14 ‰ and δ^{41}K isotopic compositions ranging from −0.35 to −0.08 ‰, again most samples indistinguishable outside of error bars, but the concentrations range largely from 0.5 to 7.0 μg/g for Rb and 198 to 1473 μg/g for K.

The Rb and K isotopic variations of CCs are relatively small, +0.03 to +0.19 ‰ for δ^{87}Rb and −0.46 to −0.04 ‰ for δ^{41}K. In contrast, the NCs (OCs and ECs) display much larger isotopic variations, from −1 to +0.3 ‰ for δ^{87}Rb and −0.9 to −0.15 ‰ for δ^{41}K (meteorite find Atlanta excluded). The elemental abundances of CCs range from 1.0 to 2.1 μg/g for Rb and 256 to 491 μg/g for K, and NCs vary between 1.8 and 4.8 μg/g for Rb and between 552 and 1059 μg/g for K (Table 1). The elemental variations in chondrites are much less than that in the differentiated planetary bodies because chondrites did not experience magmatic differentiation, but the isotopic compositions of NCs, in particular OCs, vary significantly and extend to extremely light values (Fig. 1 and Table 1).

Some NC meteorites measured in this study were also measured previously for their K and Rb isotopic compositions. Ku and Jacobsen (2020) reported δ^{41}K values for Abee (EH4) and Indarch (EH4) of −0.34 ± 0.03 ‰ and −0.38 ± 0.04 ‰, respectively, which compare well with the values that we have obtained (−0.29 ± 0.04 ‰ and −0.37 ± 0.04 ‰, respectively). Pringle and Moynier (2017) reported δ^{87}Rb values for Abee (EH4), Indarch (EH4), and Krymka (LL3.2) of −0.01 ± 0.03 ‰, −0.14 ± 0.03 ‰, and −0.37 ± 0.02 ‰, respectively. For Indarch and Krymka, their values agree well with ours (−0.08 ± 0.03 ‰ and −0.41 ± 0.04 ‰, respectively). The δ^{87}Rb value that we measured in Abee is however significantly different (−0.24 ± 0.02 ‰), which could be due to sample heterogeneity.

To investigate whether there is a good correlation between Rb and K, K in individual samples is plotted against Rb, both elementally and isotopically, in Fig. 2. Elementally, K and Rb show a great correlation, with some NC samples of higher metamorphic grades falling off the correlation (Fig. 2A). Interestingly, the samples that fall off the K-Rb elemental correlation also plot off the isotopic trend between K and Rb (Fig. 2B). This suggests that thermal metamorphism on chondrite parent bodies has decoupled the two systems, which is probably because both Rb and K are highly fluid mobile and thermally labile (the possible parent-body processes that have caused the decoupling are discussed in Sect. 5). Another notable feature about the K and Rb isotopic compositions is that for the OCs of lower metamorphic grades (types 3 and 4), the isotopic compositions show large scatter (Fig. 2B). This scatter might reflect to some extent initial heterogeneity on OC parent body. More specifically, OCs are heterogeneous agglomerates of matrix materials, chondrules of different generations, and some igneous alkali-rich lithic fragments (e.g., Wlotzka et al., 1983; Yokoyama et al., 2017), which can cause isotopic heterogeneity that is beyond the

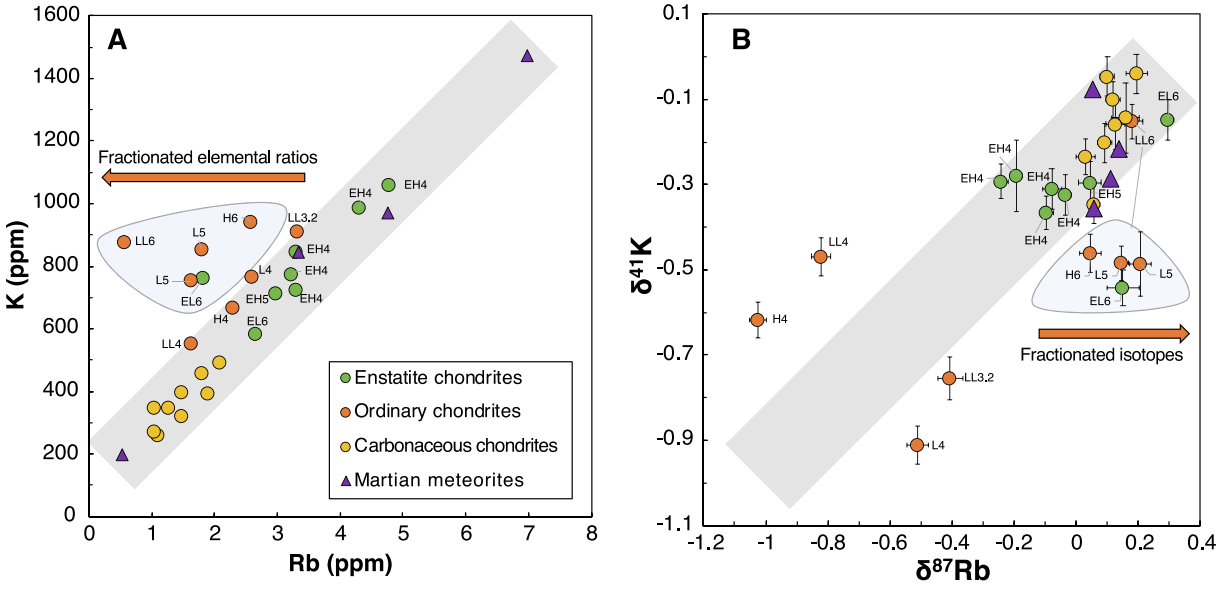

Fig. 2. The correlations between K and Rb elemental concentrations (A) and between K and Rb isotopic compositions (B) of chondritic and Martian samples. Samples of higher metamorphic grades plot off both the elemental and the isotopic trends, suggesting that parent-body processes have decoupled K and Rb.

current sampling mass. At bulk planetary scale, Rb and K show great correlations both elementally and isotopically, suggesting a volatility control of the isotopic fractionations of the two elements during planetary accretion and formation (see below).

4. Rb and K isotopic compositions of bulk planetary bodies

4.1. Rb and K isotopic compositions of bulk Earth, Moon, and Mars

Earth. The Rb and K isotopic compositions of Earth were assessed previously by several studies (Ku and Jacobsen, 2020; Nie and Dauphas, 2019; Tuller-Ross et al., 2019; Wang and Jacobsen, 2016a). Our Rb isotopic measurements of terrestrial reference materials (Nie et al., 2021a, 2021c; Nie and Dauphas, 2019) show that the basaltic samples overall have heavier δ^{87}Rb values (–0.16 ~ –0.10 ‰) than the granitic ones (–0.24 ~ –0.18 ‰) (Table 1), suggesting that magmatic differentiation or late-stage fluid exsolution could potentially fractionate Rb isotopes, as proposed by Nie and Dauphas (2019) and Hu et al. (2022). A correlation between Rb isotopic compositions and the La/U ratios of terrestrial samples was observed and was interpreted as a magmatic differentiation trend (Nie and Dauphas, 2019). The correlation gives a Rb isotopic composition of **−0.13 ± 0.01** ‰ for the Earth at the La/U ratio of CI chondrites (~27.6), which is presumably the same as the bulk Earth given that La and U are both highly refractory (Nie and Dauphas, 2019). For K isotopes, Wang and Jacobsen (2016a) estimated the bulk silicate Earth to be −0.48 ± 0.03 ‰ by averaging three terrestrial geostandards. The isotopic reference standard used in that study (Suprapur) might be isotopically lighter than the SRM3141a used here and in other studies by about 0.047 ‰ (Ku and Jacobsen, 2020). Correcting for this shift, the δ^{41}K value of the bulk silicate Earth would be −0.53 ± 0.03 ‰ relative to SRM3141a based on that study. This value is consistent with the value of −0.46 ± 0.13 ‰ reported by Ku and Jacobsen (2020) by averaging three geotandards. The study that used the most samples to constrain Earth's K isotopic composition was done by Tuller-Ross et al. (2019), who analyzed 51 geochemically diverse oceanic basalts, including mid-ocean ridge basalts, arc basalts, and oceanic island basalts, and found limited variations of K isotopic compositions among these samples. They calculated an average value of −0.43 ± 0.17 ‰ (2 s.d.) based on pristine samples and used it to represent bulk silicate Earth. Later, Hu et al. (2021b) investigated the K isotopic compositions of samples formed during differentiation and solidification of the Kilauea Iki lava lake, and found minimal K isotopic fractionation during magmatic fractionation and proposed an average of −0.42 ± 0.07 ‰ for bulk silicate Earth. Our measured K isotopic compositions of five terrestrial geostandards, together with the four geostandards reported in our previous studies (Nie et al., 2021a, c), collectively define a weighted mean (the reciprocals of the squares of the analytical uncertainties were used as weights) and error of **−0.44 ± 0.02** ‰, consistent with the values estimated by Tuller-Ross et al. (2019) and Hu et al. (2021b). Unlike Rb, the K isotopic compositions among basaltic geostandards and granitic geostandards do not show much difference (i.e., negligible magmatic differentiation; Table 1).

Moon. Pringle and Moynier (2017) measured the Rb isotopic compositions of seven lunar samples including three low-Ti and three high-Ti basalts and one cataclastic norite, yielding an average δ^{87}Rb value of +0.05 ± 0.12 ‰. Nie and Dauphas (2019) measured another five lunar basalts and one norite sample. Combining the Rb isotopic data from both studies and accounting for possible Rb isotopic fractionation during magmatic differentiation using La/U ratios, Nie and Dauphas (2019) estimated that δ^{87}Rb value of the Moon was **+0.03 ± 0.03** ‰. For K isotopes, Tian et al. (2020) measured 19 lunar rocks and lunar meteorites with various petrographic types, among which the low-Ti and high-Ti basalts show indistinguishable δ^{41}K values, defining an average of −0.07 ± 0.09 ‰. We measured the isotopic compositions of the K cuts of the same sample digestions that were previously measured for Rb (Nie and Dauphas, 2019). The samples show limited K isotopic variations among low-Ti, high-Ti, and norite samples (Table 1 and Fig. 1), with a weighted δ^{41}K mean and error of **−0.01 ± 0.02** ‰. The value agrees within error with the value −0.07 ± 0.09 ‰ reported by Tian et al. (2020) but is slightly on the heavy side.

Mars. We measured four Martian meteorite falls. The data hint at the presence of a correlation between Rb isotopic compositions and the La/U ratios in these samples (Fig. 3A), possibly due to Rb isotopic fractionation during magmatic differentiation (partial melting or fractional crystallization during Martian mantle

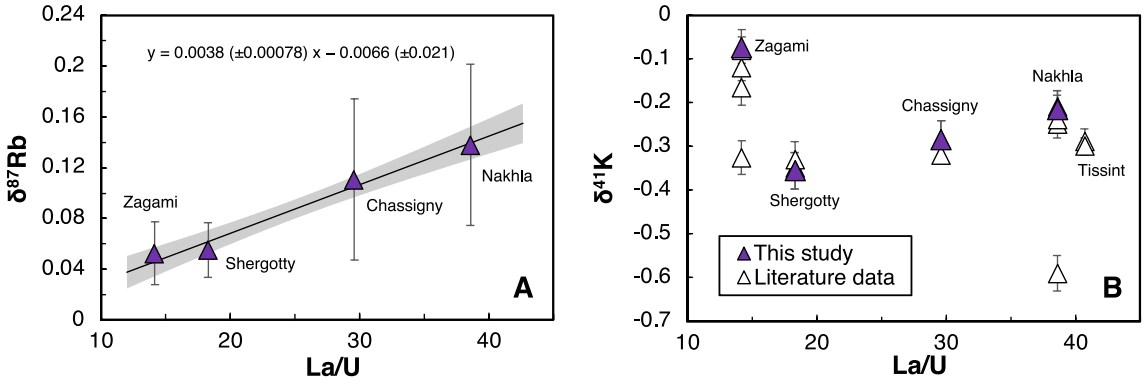

Fig. 3. Rubidium and potassium isotopic compositions of Martian meteorites. The samples shown here are only meteorite falls, from this study and the literature (Table 2). (A) Rb isotopic compositions show a good correlation with the La/U ratios of the samples, which could reflect a magmatic differentiation trend. The Rb isotopic composition of the bulk silicate Mars can be obtained by taking the Rb isotopic composition at a La/U ratio of 27.6 (the ratio of CI chondrites that presumably represents that of bulk silicate Mars), that is, +0.10 ± 0.03 ‰. (B) The K isotopic compositions of Martian samples do not show a clear trend. The K isotopic composition of the bulk silicate Mars, calculated as weighted mean ± 95 % c.i., is −0.26 ± 0.05 ‰.

differentiation). By interpolating to a La/U (g/g) ratio of 27.6 (the CI chondrite value that presumably represents that of bulk silicate Mars; Nie and Dauphas, 2019; Dauphas et al., 2022), a δ^{87}Rb value of **+0.10 ± 0.03** ‰ was obtained for bulk silicate Mars (Fig. 3A and Table 1). This value is identical to the arithmetic mean (+0.09 ± 0.08 ‰; error indicates 2 s.d.) and the weighted mean (+0.06 ± 0.04 ‰; error indicates 95 % c.i.) of the Martian samples within error. For K isotopes, no clear trend between K isotopic compositions and the La/U ratio was observed (Fig. 3B). The K isotopic compositions of Martian samples have been measured in two previously studies (Ku and Jacobsen, 2020; Tian et al., 2021). The values obtained in this study agree well with previously reported data (Fig. 3B). Taking all the sample data together (Table 2), we calculated the weighted mean and 95 % c.i. to represent the δ^{41}K value of bulk Mars, which is **−0.26 ± 0.05** ‰.

4.2. Rb and K isotopic compositions of chondrite parent bodies

Nie et al. (2021a) studied Rb and K isotopic variations in carbonaceous chondrites (CCs) and constrained the isotopic compositions of subgroup CCs (CI, CM, CV, and CO). The data are best explained as resulting from mixing between CI-like matrix and isotopically fractionated chondrules with light K and Rb isotopic compositions (Jiang et al., 2021; Nie et al., 2021a). Modeling shows that this light K and Rb isotope enrichment in chondrules can be explained by evaporation in a saturated medium, followed by rapid cooling and incomplete condensation onto chondrules from a supersaturated medium, imparting a dominant light isotope enrichment to the chondrules (Nie et al., 2021a). The Rb isotopic compositions of the matrix and chondrule end members were estimated to be δ^{87}Rb = +0.19 ± 0.03 ‰ and +0.04 ± 0.05 ‰ respectively, and the K isotopic compositions were estimated to be δ^{41}K = +0.04 ± 0.08 ‰ and −0.33 ± 0.12 ‰, respectively (Nie et al., 2021a). The same model can potentially explain the isotopic variations observed for other MVEs in CCs (e.g., Te and Zn; Luck et al., 2005; Hellmann et al., 2020). The Rb and K isotopic compositions of bulk CI, CM, CV, and CO from Nie et al. (2021a) are listed in Table 1.

Unlike differentiated bodies and CCs, the isotopic compositions of NCs are more variable and not systematic. ECs and OCs show substantial within-group isotopic variations, especially for Rb in OCs (Table 1; Figs. 1, 4, and 5). Large isotopic variations in NCs have

Table 2
Rubidium and potassium isotopic compositions of Martian meteorite falls.

Sample	Type	La/U[a]	$\delta^{87/85}$Rb (‰)	95 % c.i.	$\delta^{41/39}$K (‰)	95 % c.i.	Ref.
Shergotty	Shergottite	18.3	0.055	0.021	−0.356	0.042	This study
					−0.350	0.020	Tian et al. (2021)
					−0.330	0.040	Tian et al. (2021)
Zagami	Shergottite	14.2	0.052	0.025	−0.075	0.042	This study
					−0.120	0.030	Tian et al. (2021)
					−0.080	0.030	Tian et al. (2021)
					−0.326	0.038	Ku and Jacobsen (2020)
					−0.167	0.038	Ku and Jacobsen (2020)
Tissint	Shergottite	40.7			−0.290	0.030	Tian et al. (2021)
					−0.300	0.020	Tian et al. (2019)
Chassigny	Chassignite	29.6	0.111	0.063	−0.285	0.042	This study
					−0.320	0.020	Tian et al. (2021)
Nakhla	Nakhlite	38.6	0.138	0.063	−0.216	0.042	This study
					−0.590	0.040	Tian et al. (2021)
					−0.250	0.030	Tian et al. (2021)
					−0.240	0.029	Ku and Jacobsen (2020)
					−0.211	0.029	Ku and Jacobsen (2020)
Bulk silicate Mars			0.098	0.030	−0.261	0.047	

a. La/U ratios are from The Martian Meteorite Compendium (https://curator.jsc.nasa.gov/antmet/mmc/) and Balta et al. (2015).

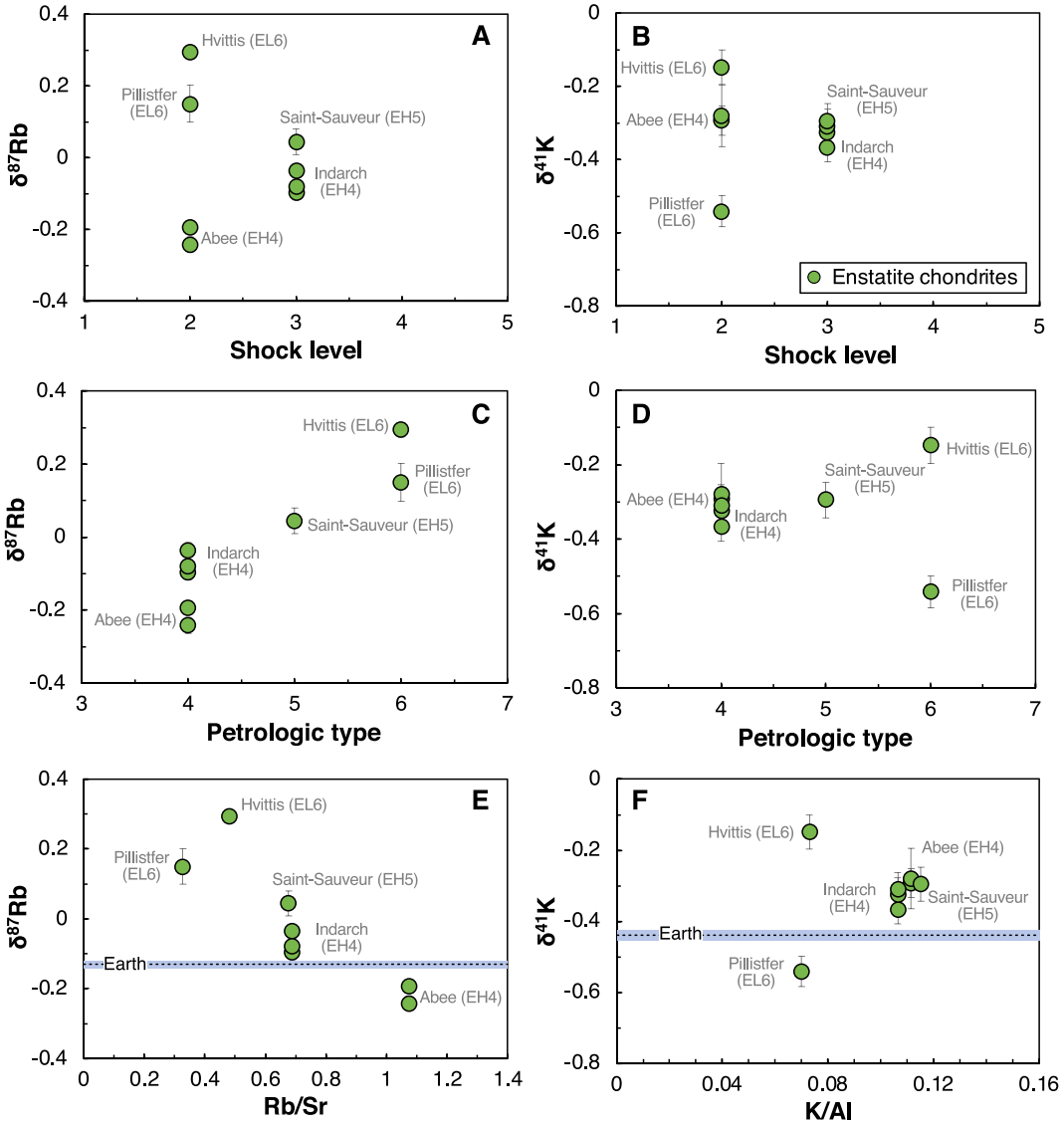

Fig. 4. Rubidium and potassium isotopic compositions of enstatite chondrites, plotted against the shock levels of the samples (A and B; Table S1), the petrologic types (C and D), and the Rb/Sr and K/Al ratios (E and F).

also been observed for other volatile elements such as Zn (Luck et al., 2005; Moynier et al., 2011), Te (Fehr et al., 2018; Hellmann et al., 2021), and Cd (Wombacher et al., 2008). In Figs. 4 and 5, we plot Rb and K isotopic compositions of ECs and OCs against shock levels (Table S1; Britt and Pieters, 1991; Stöffler and Keil, 1991; Rubin et al., 1997; Friedrich et al., 2004, 2017; Rubin, 2015; Bischoff et al., 2018), petrologic types, and Rb/Sr and K/Al ratios. The EC subgroups EH and EL were presumably derived from separate parent bodies and experienced different geological histories (e.g., Sears et al., 1982), but due to the limited number of samples that have been studied, we do not distinguish the two subgroups. This should be acceptable when considering the bulk isotopic compositions of the bodies, because for other MVEs such as Te (Hellmann et al., 2021), Zn (Moynier et al., 2011), and Cd (Wombacher et al., 2008), no clear distinction was found between the isotopic compositions of EHs and ELs. This is also the case for OCs, for which the subgroups H, L, and LL seem to show similar ranges of isotopic variations for Te (Hellmann et al., 2021), Zn (Luck et al., 2005), Cd (Wombacher et al., 2008), and K (Ku and Jacobsen, 2020). The plots in Figs. 4 and 5 show no clear correlations or systematic variations, except in ECs where there seem to be trends between Rb isotopic compositions and petrologic type and Rb/Sr ratios. Given the small number of samples, it is unknown how robust the trends are, but if real, the trends would suggest volatilization and migration of Rb during EC parent-body processes.

To constrain the bulk Rb and K isotopic compositions of OC and EC parent bodies, we have used the kernel density estimates (KDEs) to show the distributions of δ^{87}Rb and δ^{41}K of samples from this study and from literature [data from the literature (Pringle and Moynier, 2017; Bloom et al., 2020; Ku and Jacobsen, 2020) are compiled in Table S2]. Only meteorite falls were considered to minimize the effect of potential terrestrial weathering/contamination. NCs show large intra- and inter-sample isotopic variations for Rb and K (Table S2). At the current stage, it cannot be determined that intra-sample isotopic variations are significantly smaller than inter-sample variations. Therefore, we treated the data of different pieces of a same meteorite as individual data points when plotting

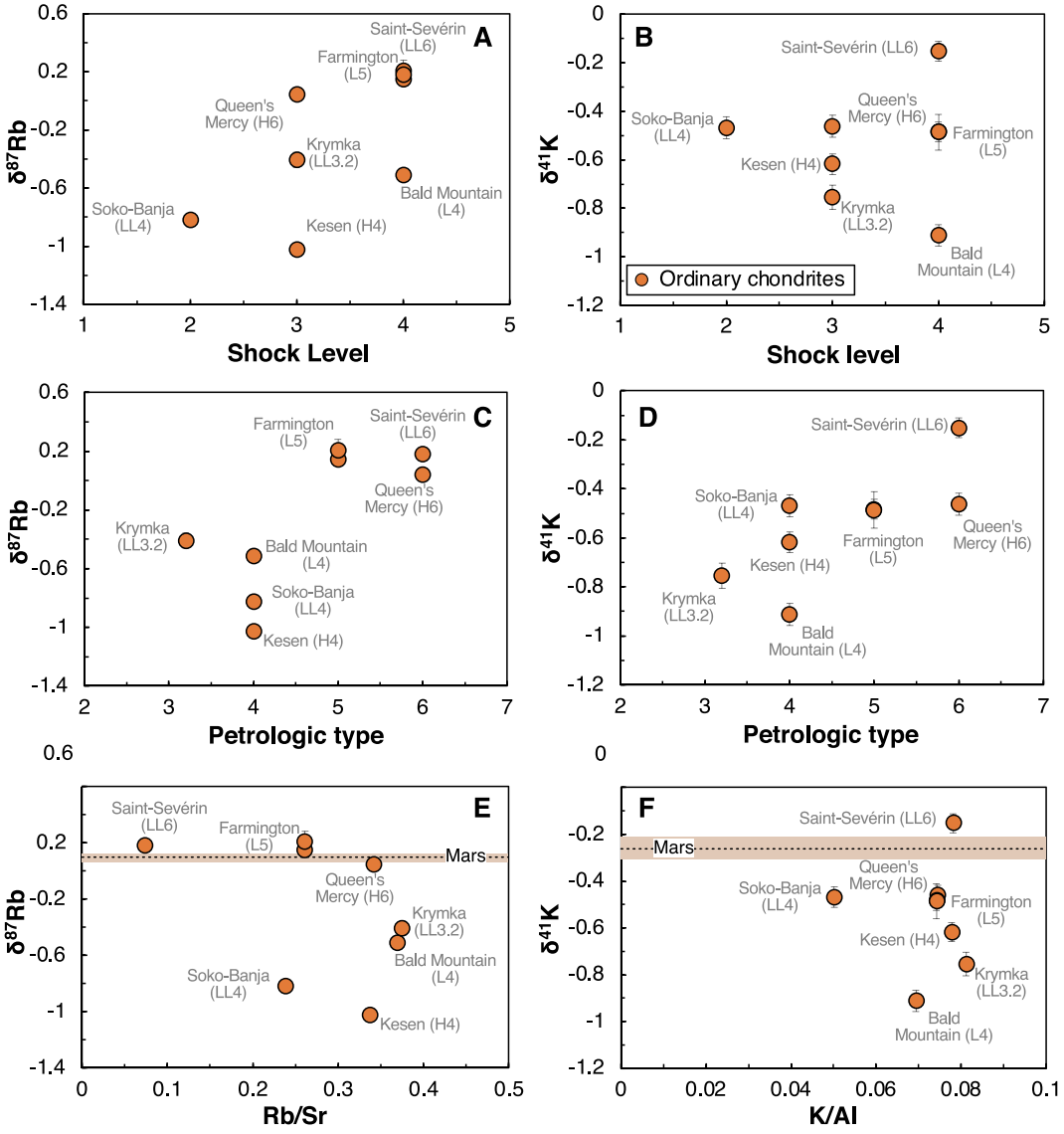

Fig. 5. Rubidium and potassium isotopic compositions of ordinary chondrites, plotted against the shock levels of the samples (A and B; Table S1), the petrologic types (C and D), and the Rb/Sr and K/Al ratios (E and F).

the probability density functions (PDFs), but average values were used for duplicate measurements of the same homogenized aliquots (Table S2).

For each meteorite group, the KDEs of less metamorphosed meteorites (types 3 and 4; red curve in Fig. 6), more metamorphosed ones (types 5 and 6; blue curve), and all samples together (types 3, 4, 5, and 6; black dashed curve) are shown (Fig. 6). The samples of low and high metamorphic grades were plotted separately to see whether there is statistical difference between less and more metamorphosed samples. Many of the distributions are multimodal and we were interested in evaluating the value of the highest mode and its uncertainty, which was done by bootstrapping the data. For bootstrapping, the same number of data points as that of the original data set were resampled randomly 100,000 times, and the mode of each resampled data set was recorded. If there were two modes with equal probability, the mode that is closer to the mean of the original data was chosen. This leads to a total number of 100,000 modes for the 100,000 resampled data sets, and the KDE of the modes was plotted (grey curves in Fig. 6). Then the mode of the bootstrapping KDE was used to represent the bulk composition of the meteorite group, and the 0.025 and 0.975 quantiles were used to represent the lower and upper bound of the error (i.e., 95 % c.i.). A bandwidth of 0.05 was used to smooth the bootstrapping curve. The bandwidth is similar to the automatically computed bandwidth in Mathematica, and the two bandwidths yielded consistent results. The calculated modes and 95 % c.i. values are labeled next to the bootstrapping curves (Fig. 6). For K isotopes, subgroups of H, L, and LL were also plotted (Fig. 6A–C). For Rb isotopes, subgroups were not plotted because of limited number of data points.

The modes of δ^{41}K in OCs and ECs are $-0.72^{+0.28}_{-0.41}$ ‰ (95 % c.i.) and $-0.33^{+0.37}_{-0.23}$ ‰ (Fig. 6D and E). The OC subgroups H, L, and LL have similar δ^{41}K modes, and all of them are identical to the bulk OCs within error (Fig. 6A–C). Potassium isotopes do not show clear differences between less and more metamorphosed samples (Fig. 6A–E), although the more metamorphosed samples seem to show more dispersion in their K isotopic compositions. The modes in δ^{87}Rb of OCs and ECs are $+0.05^{+0.20}_{-1.09}$ ‰ (95 % c.i.) and $+0.02^{+0.29}_{-0.26}$ ‰ (Fig. 6F and G), respectively, with the former poorly defined due to

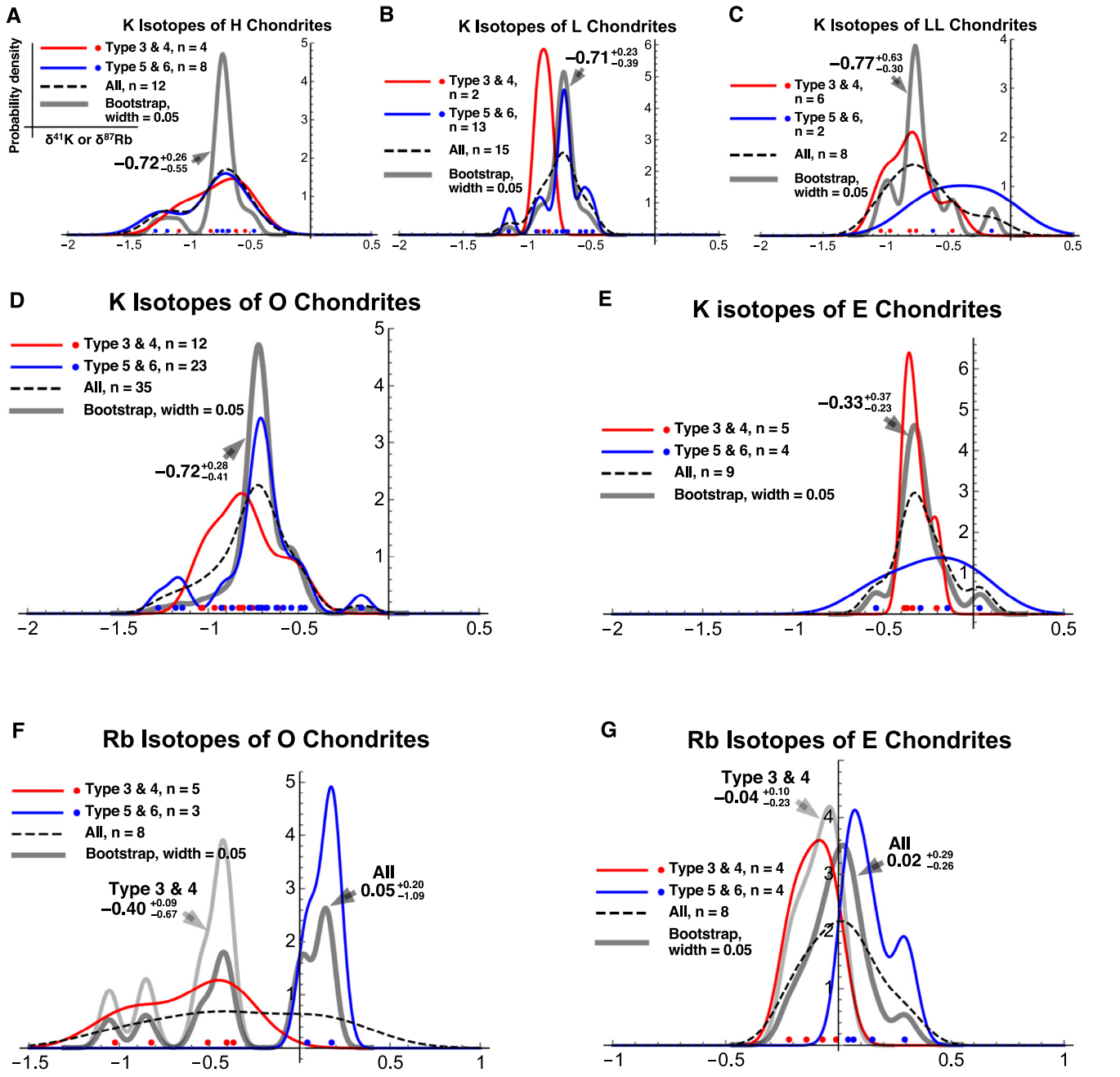

Fig. 6. Kernel density estimates (KDEs) of Rb and K isotopic compositions of bulk NCs. Panels A, B, and C show K isotopic compositions of H, L, and LL chondrites, panels D and E show the K isotopic compositions of bulk OCs and ECs, and panels F and G show the Rb isotopic compositions of bulk OCs and ECs, respectively. In each panel, the less metamorphosed samples (types 3 and 4; red dots and curves), more metamorphosed samples (types 5 and 6; blue dots and curves), and all samples together are plotted separately for comparison. Bootstrapping was used to constrain the bulk isotopic compositions and the results are shown in grey curves. The estimated bulk compositions and their 95 % c.i. are labeled next to the bootstrapping curves and reported in Table 1. (For interpretation of the references to colour in this figure legend, the reader is referred to the web version of this article.)

the large dispersion in the data (below we use another method to constrain the δ^{87}Rb of OCs). The more metamorphosed samples seem to show heavier Rb isotopic compositions than less metamorphosed ones (Fig. 6F and G). Using either types 3 and 4 or all the samples to estimate the bulk δ^{87}Rb yield similar values for ECs. For OCs, however, using types 3 and 4 yields a much lower value than using all the samples. A caveat however is that the total number of samples for Rb is small, and some samples are pieces from a same meteorite (Table S2). More samples are needed to test whether the more metamorphosed samples are systematically shifted towards heavier Rb values.

4.3. Rb isotopic composition of OC parent body(ies) constrained from vapor saturation level during Mars formation

Isotopic anomalies can help establish genetic ties between meteorite groups and planets (Clayton, 1993; Dauphas and Schauble, 2016). Isotopic anomalies of refractory elements suggest

that Earth and Mars received those elements from the NC reservoir (Dauphas 2017; Burkhardt et al., 2021). The isotopic anomalies of MVE Zn suggest ~ 70 % of Zn in Earth from the NC reservoir and the rest from the CC reservoir (Savage et al., 2022; Steller et al., 2022), which is consistent with Earth's volatile element concentration pattern (Braukmüller et al., 2019). K and Rb are less volatile than Zn, and the terrestrial planets should have them mainly from the NC reservoir. For Earth, the most likely building blocks would be material similar to ECs isotopically but with a different chemical composition, most notably a much higher Mg/Si ratio (Dauphas et al., 2015; Dauphas, 2017). The bulk K isotopic composition of the Earth (–0.44 ± 0.02 ‰; Table 1) is similar to the mode value for ECs ($-0.33^{+0.37}_{-0.23}$ ‰, Table 1 and Fig. 6E) and this is also the case for Rb isotopes (–0.13 ± 0.01 ‰ for Earth and $+0.02^{+0.29}_{-0.26}$ ‰ for ECs; Table 1 and Fig. 6G). This suggests that the processes that caused volatile depletion in Earth did not fractionate Rb and K isotopes significantly.

The most plausible building blocks of Mars isotopically are OCs and ECs. Although the exact mixing proportions are still debated (Lodders and Fegley, 1997; Sanloup et al., 1999; Tang and Dauphas, 2014; Fitoussi et al., 2016; Brasser et al., 2018), OCs should have contributed significantly. Assuming that OCs are the major building blocks of Mars, we can compare the isotopic compositions of the two. The K isotopic composition of Mars (–0.26 ± 0.05 ‰) is distinctively higher than the mode value of OCs ($-0.72^{+0.28}_{-0.41}$ ‰). The bulk Rb isotopic composition of OCs could not be constrained accurately using KDE due to the large isotopic variation (from –1 to + 0.2 ‰; Table 1; Fig. 6F). However, one can attempt to use the K isotopic fractionation between Mars and OCs to estimate Rb isotopic fractionation between the two bodies, and then the bulk Rb isotopic composition of OCs can be calculated more accurately given that the Rb isotopic composition of Mars is well constrained. Using K isotopic fractionation to estimate Rb isotopic fractionation hinges on the fact that the two elements should have the same level of vapor saturation ($S=P/P_{sat}$; vapor pressure divided by saturation or equilibrium vapor pressure) during the volatilization processes of Mars accretion and possibly magma ocean. Following Nie and Dauphas (2019) and assuming that volatile loss from Mars can be described with a Raleigh-type distillation process, the isotopic fractionation for each element i between the evaporation residue (Mars) and the original isotopic composition (OCs) can be expressed as,

$$\Delta_i = [\Delta^{v-l}_{eq,i} + (1 - S_i)\Delta^{v-l}_{kin,i}] \ln f_i \quad (3)$$

where $\Delta^{v-l}_{eq,i}$ is the equilibrium isotope fractionation between the vapor and the evaporating liquid for element i, S_i is the saturation level of i in the vapor, f_i is the fraction of i remaining in the residue after evaporation, and $\Delta^{v-l}_{kin,i}$ is the kinetic isotopic fractionation between the vapor and the evaporating liquid, and takes the form,

$$\Delta^{v-l}_{kin,i} = 1000\left(\frac{\gamma_{i2}}{\gamma_{i1}}\sqrt{\frac{m_{i1}}{m_{i2}}} - 1\right) \quad (4)$$

where γ is the evaporation coefficient, $i1$ and $i2$ are the two considered isotopes of i, and m_{i1} and m_{i2} their respective mass. In this case the considered isotopic ratio in δ notation would be $i2/i1$, i.e., usually a heavier isotope divided by a lighter isotope. Assuming the equilibrium isotopic fractionation factor $\Delta^{v-l}_{eq,i}$ is known (at high temperature the value is close to 0), and that the evaporation coefficients are the same for both isotopes, then the saturation level S_i can be calculated for each element provided that the Δ_i (the observed isotopic fractionation between Mars and OCs) is measured. In turn, if the saturation level S_i is known, the isotopic fractionation Δ_i could be calculated. The heavier K isotopic composition of Mars (–0.26 ± 0.05 ‰) compared to OCs ($-0.72^{+0.28}_{-0.41}$ ‰) suggests evaporation of K into a undersaturated vapor medium. The equilibrium K isotope fractionation between K-bearing minerals have been investigated using first-principles calculations (Li et al., 2019b, c; Zeng et al., 2019). Using plagioclase as a proxy for melt, the equilibrium K isotope fractionation factor between vapor and melt is –0.07 ‰ at 2000 K [$\Delta^{v-l}_{eq,K} = (-286,000 \pm 143,000)/T^2$; Zeng et al., 2019; Dauphas et al., 2022]. Using a kinetic isotope fractionation factor $\Delta^{v-l}_{kin,K}$ of –25 ‰ (Eq. (4); Zhang et al., 2021), and f_K of 0.27 [$(\frac{K}{U})_{Mars}/(\frac{K}{U})_{OC} = 0.27$; Dauphas et al., 2022], the saturation level of K S_K can be calculated to be $0.989^{+0.009}_{-0.013}$. To confirm that this level of vapor saturation is relevant to Rb, we also calculated the vapor saturation level of Zn, which has a similar volatility to Rb (half-condensation temperature of Zn is about 700 K; Lodders, 2003; Wood et al., 2019) but is more chalcophile. The Zn isotopic composition ($\delta^{66/64}$Zn) of Mars was constrained to be +0.26 ± 0.09 ‰ (Paniello et al., 2012). Using the compiled Zn isotopic data of OCs (Table S2; Luck et al., 2005; Moynier et al., 2007, 2011; Paniello, 2013), we estimate the bulk Zn isotopic composition to be $+0.10^{+0.98}_{-0.46}$ ‰ using the kernel density estimates. Assuming the equilibrium and kinetic isotopic fractionations between vapor and melt of –0.06 ‰ ($\Delta^{v-l}_{eq,Zn} = -254,000/T^2$; Dauphas et al., 2022) and –15.38 ‰, respectively, and f_{Zn} of 0.54 [$(\frac{Zn}{Lu})_{Mars}/(\frac{Zn}{Lu})_{OC} = 0.54$; Wasson and Kallemeyn, 1988; Yoshizaki and McDonough, 2020], the saturation level of Zn (S_{Zn}) was calculated to be $0.987^{+0.013}_{-0.048}$, and is consistent with the calculated saturation level of K (Fig. 7).

Applying the saturation level of K ($0.989^{+0.009}_{-0.013}$) to Rb, and assuming an equilibrium Rb isotopic fractionation of –0.016 ‰ at 2000 K [$\Delta^{v-l}_{eq,Rb} = (-62,000 \pm 143,000)/T^2$; Zeng et al., 2019; Dauphas et al., 2022], a kinetic isotope fractionation $\Delta^{v-l}_{kin,Rb}$ of –11.63 ‰, f_{Rb} of 0.21 [$(\frac{Rb}{Sr})_{Mars}/(\frac{Rb}{Sr})_{OC} = 0.21$; Dauphas et al., 2022], and a bulk Mars Rb isotopic composition of +0.26 ± 0.09 ‰ (Table 1), the bulk Rb isotopic composition of OCs is estimated to be $-0.12^{+0.15}_{-0.24}$ ‰ (Table 1 and Fig. 7). We prefer using this value to represent the OC parent body(ies) because the value is more precise, while the large dispersion in Rb isotopic compositions of individual OCs precludes an accurate estimate of the bulk using

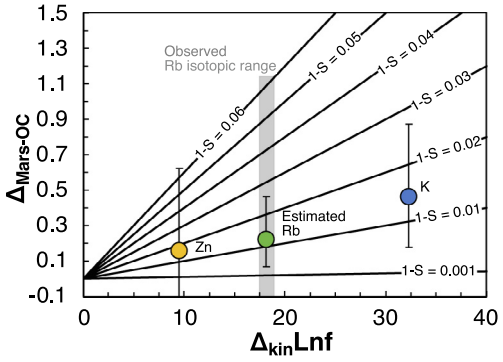

Fig. 7. Vapor saturation level during Mars formation. The K isotopic difference between bulk Mars and OCs (the blue filled circle) is consistent with a vapor saturation level (S) of $0.989^{+0.009}_{-0.013}$. The Zn isotopic fractionation (the yellow filled circle) suggests a consistent vapor saturation level of $0.987^{+0.013}_{-0.048}$. Thus, this saturation level should be applicable to Rb isotopes. The observed Rb isotopic variation in OCs is too large to obtain an accurate estimate of Mars-OC isotopic fractionation (the grey vertical bar). By assuming that the vapor saturation level of Rb is the same as that of K, the Rb isotopic fractionation between bulk Mars and OCs (the green filled circle) could be better constrained, and thus the bulk Rb isotopic composition of OCs could be constrained and was calculated to be $-0.12^{+0.15}_{-0.24}$ ‰ (Table 1). (For interpretation of the references to colour in this figure legend, the reader is referred to the web version of this article.)

the KDE method above (Sect. 4.2; Fig. 6F). Further work is needed to validate this value by measuring largely homogenized powder samples of OCs.

4.4. Correlation between K and Rb isotopic compositions of bulk planetary bodies

The K and Rb isotopic compositions of bulk planetary bodies can provide clues on the conditions that prevailed during depletion of MVEs from planetary building blocks. In Fig. 8, we plot K against Rb for bulk planetary bodies, whose isotopic compositions were constrained in previous sections. Clear correlations are observed for both elemental concentrations and isotopic compositions. The elemental correlation between K/U and Rb/Sr (volatile/refractory ratios normalized to CI chondrties) has been observed previously by Halliday and Porcelli (2001), Davis (2006), and Dauphas et al. (2022) (Fig. 8A). The two ratios reflect the degree of volatile depletion in planetary bodies, suggesting possible volatile loss during planetary formation. The isotopic compositions of K and Rb also show a trend (Fig. 8B). This trend is also reflected by the K and Rb isotopic trend among individual samples (Fig. 2B).

Potassium and rubidium isotopic correlation was observed in CCs, and the correlation was used by Nie et al. (2021a) for arguing against a nucleosynthetic origin of $^{41}K/^{39}K$ isotopic variations among planetary bodies (Ku and Jacobsen, 2020). This is because for nucleosynthetic anomalies one would not expect to see a correlation given that K isotopes and Rb isotopes are produced by different nucleosynthetic processes at different stellar sites, and thus a correlation must reflect mass-dependent processes. We show here that the correlation is not just for CCs, but a broader trend exists among planetary bodies. This again argues against the nucleosynthetic origin of K isotopic variations, and supports a volatility control (evaporation and condensation processes) of the isotopic variations. Further evidence that supports volatility-controlled isotopic fractionation is that the slope of the correlation is close to the kinetic isotope fractionation slope (i.e., $\ln(39/41)/\ln(85/87) = 2.15$) (Fig. 8B) during evaporation and condensation processes. Despite of the elemental and isotopic correlations, the elemental vs isotopic compositions for each element is decoupled. Although both incomplete evaporation and condensation can cause volatile depletion, the directions of isotopic fractionations for the two processes are opposite. More specifically, evaporation would enrich heavy isotopes in the solid/liquid residue while condensation would enrich light isotopes in the condensed solid/liquid. The lack of correlation between elemental and isotopic compositions therefore suggests that the planetary bodies were not formed through a single stage evaporation or condensation process, but multiple evaporation and condensation processes and variable amounts of evaporation/condensation of building materials must have occurred. The parent bodies of OCs and ECs have lighter Rb and K isotopic compositions compared to CI chondrites, but this could not be explained by a simple condensation scenario. To obtain light isotopic composition during condensation one would expect Rb and K to be depleted in the condensates (i.e., incomplete condensation), but the OCs and ECs are not depleted in the two elements compared to CI chondrites (Fig. 8A).

5. Possible parent-body processes that caused isotopic variations in individual NC samples

While CCs show clear systematic correlations between isotopic compositions and matrix/chondrule proportions for Rb and K, implying mixing between matrix and chondrule reservoirs (Nie et al., 2021a), mixing cannot explain the isotopic variations in OCs and ECs, for which the proportions of chondrules vary much less than in CCs (~65–75 vol% in OCs and 15–20 vol% in ECs, in contrast to ~ 0–55 vol% in CCs; Rubin, 2000). Clearly, other processes must have caused the large Rb and K isotopic variations in OCs and ECs. The possible processes include (i) initial heterogeneities in meteorite constituents, (ii) volatile loss during parent-body thermal metamorphism, (iii) element diffusion during thermal metamorphism, and (iv) shock heating during impacts. We discuss these processes in the following sections.

5.1. Sample heterogeneity: how much mass is representative?

The measured Rb and K isotopic compositions of OC samples show large isotopic variations (−1.02 to +0.21 ‰ for Rb and −0.91 to −0.15 ‰ for K). The digested sample masses in this study are around 100 mg, and the samples are usually from homogenized powders of 200 mg or more. The large intra- and inter-sample isotopic variations suggest that the sample masses used in this study might not be enough for getting a representative

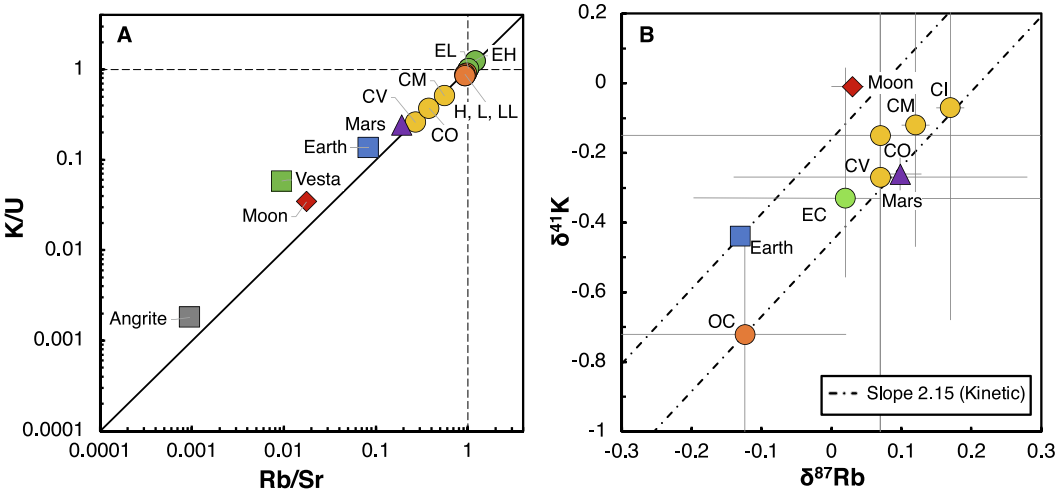

Fig. 8. Potassium and rubidium elemental and isotopic correlations among planetary bodies. (A) the elemental correlation. The K/U and Rb/Sr ratios are from Dauphas et al. (2022). (B) the isotopic correlation. The trend has a slope close to the kinetic evaporation/condensation slope of 2.15, suggesting a volatility control on the K and Rb isotopic fractionation, rather than nucleosynthetic anomalies.

bulk isotopic composition. A possible cause in this respect is the presence of chondrules that have fractionated K (and presumably Rb) isotopic compositions relative to bulk hand specimen; a phenomenon known as nugget effect (Dauphas and Pourmand, 2015). In this section we calculate the typical mass that is needed for mitigating the influence of chondrule nugget effect.

A distinct feature of OCs is that they contain large amount of chondrules (65–75 vol%; Rubin, 2000). The Rb isotopic compositions of individual chondrules have not been measured, but significant variation in K isotopic compositions has been observed (Alexander et al., 2000; Alexander and Grossman, 2005; Jiang et al., 2021), possibly due to their formation at igneous temperatures and their repeated cooling and heating histories. Chondrules in type 3 OC Bishunpur (LL3.1) and Semarkona (LL3.0) have been measured for K isotopes using in-situ SIMS method (Alexander et al., 2000; Alexander and Grossman, 2005). The measured 11 chondrules in Bishunpur have δ^{41}K values ranging from −15.5 to + 12 ‰ (Alexander et al., 2000), and the 28 Semarkona chondrules show variation of −9.5 to + 17.8 ‰ (Alexander and Grossman, 2005), much larger than the isotopic variation in OC samples. The heterogeneity in the isotopic composition of chondrules could lead to a "nugget effect", when the sampled masses are small, causing large isotopic variation at bulk sample scale.

Evidently, the higher the sampled mass, the closer the composition of the sample to the bulk composition. We therefore calculate the variations of Rb and K isotopic compositions (relative to the assumed bulk isotopic composition), as a function of sample mass. In the model, the K isotopic compositions of the 39 chondrules from Bishunpur and Semarkona were used to represent the possible compositions of chondrules. For calculating Rb isotopic compositions, we scaled down the K isotopic compositions by a factor of 2.15 [i.e., $\ln(39/41)/\ln(85/87) = 2.15$]. The L chondrite-normalized K/Al ratios of the chondrules were reported, and we estimated the Rb/Al ratios by assuming $(Rb/Al)_{chondrule}/(Rb/Al)_{bulk} = (K/Al)_{chondrule}/(K/Al)_{bulk}$. Chondrules have different sizes, and we assumed the size distribution to follow that reported by Nelson and Rubin (2002). The matrix was assumed to have the same K and Rb isotopic compositions and K/Al and Rb/Al ratios as the bulk, therefore the isotopic heterogeneity is caused only by the isotopic variation in chondrules. The chondrule mass fraction was assumed to be 0.7.

We assumed a final sample mass of 1 g, and calculated the corresponding approximate number of chondrules by dividing the sample mass by the average chondrule mass. Then the mass and isotopic compositions were randomly assigned to each chondrule. We calculated 1000 chondrite growth trajectories by assembling chondrules and matrix to the final mass. For each trajectory, the isotopic composition was tracked as the sample mass increased, until eventually the final mass was reached. Then all the 1000 trajectories were plotted together to calculate the 2 s.d. of the isotopic composition at a given sample mass.

The trajectories of isotopic composition against the sampled mass are plotted in Fig. 9 as red curves, and the 2 s.d. of the isotopic composition is plotted as blue curves. The bulk Rb and K isotopic compositions were assumed to be zero. The figure shows both Rb and K isotopic deviation as a function of the sampled mass, and the difference is solely due to the scale down of the K isotopic variations by a factor of 2.15 for Rb isotopic variations. The results show isotopic deviations from the bulk isotopic composition at low sample masses. For example, when a sample mass is 200 mg, the deviations of Rb and K isotopic compositions from the bulk are ~±0.13 ‰ and ±0.25 ‰ (2 s.d.), respectively. Given that our samples are from homogenized powders of ≥ 200 mg, this chondrule nugget effect might be accountable for some of the isotopic variations observed in individual samples, but not all of them. The total K isotopic variation in OCs is ~ 0.8 ‰ (Fig. 1), comparable to but larger than the ±0.25 ‰ calculated here. The Rb isotopic variation of ~ 1.2 ‰ is much larger than the chondrule nugget effect (±0.13 ‰), suggesting later modification of isotopic compositions by parent-body processes. Even for the most pristine OCs type 3 and 4, the Rb isotopic variation (~0.6 ‰) is larger than the chondrule nugget effect. This reflects that the isotopic heterogeneity in the samples is not only from isotopic variations in chondrules, but also from variations in other components including alkali-rich clasts and matrix. In addition, aqueous alteration has been observed in pristine OCs (for example, bleached chondrules in many type 3 OCs; Grossman et al., 2000) and could have also contributed to isotopic heterogeneity. For future sample analysis, a sample size at the gram level would be preferred in order to keep the chondrule nugget effect within the analytical precision (~0.1 ‰ for K and ~ 0.05 ‰ for Rb) (Fig. 9).

5.2. Parent-body thermal metamorphism

Parent-body thermal metamorphism can affect the isotopic compositions of K and Rb through two processes (Fig. 10): (i) these elements could possibly have been vaporized and transported, and isotopically fractionated during heating of the chondrite parent

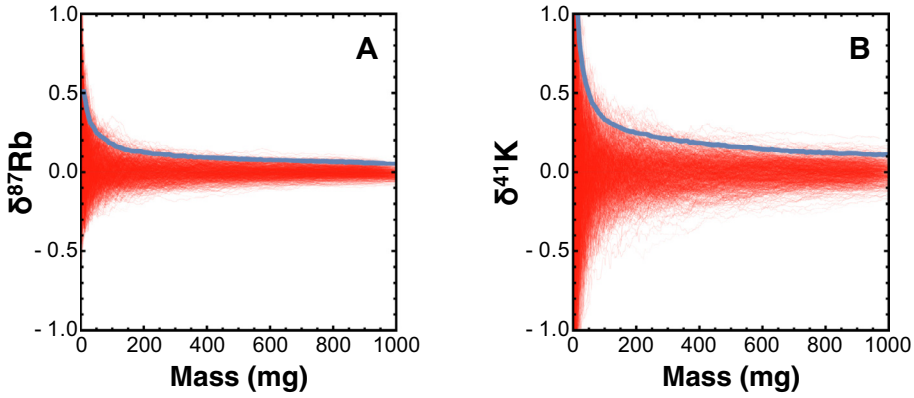

Fig. 9. Modeled isotopic deviation from the bulk sample composition as a function of sampled mass. The deviation is assumed to be due to chondrule "nugget effect" (i.e., the isotopic heterogeneity in chondrules). The model tracks the isotopic composition of a sample with ordinary chondrite-like composition during its growth by assembling chondrules and matrix. Red curves represent 1000 growth trajectories. Blue curves represent the 2 s.d. of the isotopic compositions of red curves. In order for the isotopic heterogeneity caused by chondrule "nugget effect" to be smaller than analytical uncertainties (~0.1 ‰ for K and 0.05 ‰ for Rb), a sample mass at the gram level is preferred. (For interpretation of the references to colour in this figure legend, the reader is referred to the web version of this article.)

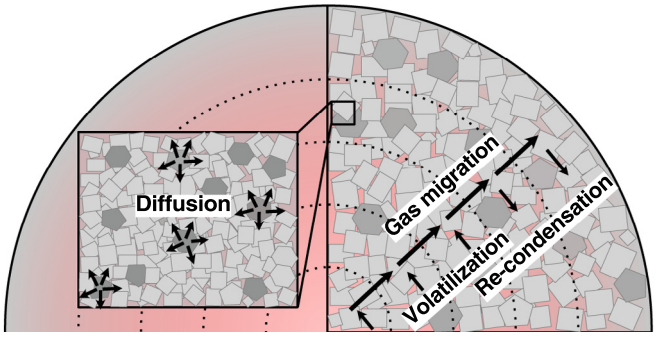

Fig. 10. Two possible processes associated with parent-body thermal metamorphism that could have caused Rb and K isotopic variations in NC samples: (i) volatilization and gas transport during heating of chondrite parent bodies by ^{26}Al decay, which is commonly invoked to explain the isotopic variations of volatile elements in NCs. The process is driven by the temperature gradient in a parent body, and volatile elements could be vaporized in the hot center area and be transported and condensed to the colder layers near the surface, and (ii) diffusive re-equilibration at the hand-specimen scale between components rich and poor in alkali elements, which could induce large kinetic isotopic fractionation.

bodies by ^{26}Al decay, or (ii) diffusive re-equilibration at the hand-specimen scale between components rich and poor in alkali elements could have induced kinetic isotopic fractionation. The first process would affect the more metamorphosed samples at bulk planetesimal scale while the second process would be a more local process affecting primarily samples that experienced intermediate or high grades metamorphism. Plotting of the Rb and K isotopic compositions against metamorphic grades show no clear trends (Figs. 4 and 5). The KDEs of Rb and K (Fig. 6) show that samples of high and low metamorphic grades do not have distinct K isotopic compositions, but seem to have different Rb isotopic compositions, with the caveat that the number of Rb samples is small. Below, we explore quantitatively through modeling the possibility of process (i), volatilization and gas transport during parent-body metamorphism, to see at what level the process could affect K and Rb isotopic fractionation (Sect. 5.2.1). The case has been made that this could be a relevant process to explain the isotopic variations of other volatile elements such as Zn, Cd, and Te in NCs (e.g., Luck et al., 2005; Wombacher et al., 2008; Moynier et al., 2011; Fehr et al., 2018; Hellmann et al., 2021). The process (ii) diffusive re-equilibration during thermal metamorphism will be discussed after in Sect. 5.2.2.

5.2.1. Volatilization and gas transport during parent-body metamorphism cannot explain the isotopic variations

Volatilization during parent-body metamorphism has been invoked to explain the large isotopic variations of volatile elements in OCs and ECs (e.g., Wombacher et al., 2008; Hellmann et al., 2021). It has been postulated that chondrite parent bodies accreted homogeneously from type 3 materials, but subsequent metamorphism led to some volatile loss (Dodd, 1969). Volatile loss during parent-body metamorphism is envisioned as transport of gaseous volatile elements (vaporized from solids into pores due to ^{26}Al heating) along the temperature gradient. Vaporized volatile elements would presumably migrate from the hot center to the cold outer part of the body, and then may be lost to space. This migration could be associated with isotopic fractionation and such a scenario has been invoked to explain the observed isotopic variations of MVEs (e.g., Luck et al., 2005; Wombacher et al., 2008; Moynier et al., 2011; Fehr et al., 2018; Hellmann et al., 2021). However, a quantitative understanding of volatile transport during this process is still lacking. For example, at what spatial scale MVEs can be transported? Would volatile elements be lost or would they condense in a cold trap inside the planetary body? How much can this process fractionate isotopes of MVEs? Here we develop a simple mathematical model to simulate the migration of Rb and K during thermal metamorphism of chondrite parent bodies.

Similar modeling has been done for highly volatile elements such as C, N, Bi, Tl, and In in chondrite parent bodies (Sugiura et al., 1986, 1987; Hashizume and Sugiura, 1998), but not for moderately volatile elements. Those previous studies showed that isotopic fractionation of highly volatile elements through this process is possible, but large uncertainties on the thermodynamic data precluded a definitive conclusion (Sugiura et al., 1986, 1987; Hashizume and Sugiura, 1998). The parameters for our modeling of Rb and K are summarized in Table S3. The model comprises two steps: (i) calculation of the thermal profile (temperature vs radius) of an assumed chondrite parent body as a function of time, with heat produced by decay of the short-lived radionuclide ^{26}Al, and conduction being the primary heat transport mechanism, and (ii) calculation of the evaporation and transport of an element, which was done numerically through a finite difference approach.

5.2.1.1. Thermal evolution of chondrite parent bodies. Following previous work on modeling thermal histories of planetesimals (e.g., Miyamoto et al., 1982; Sugiura et al., 1986; Bennett Iii and McSween Jr., 1996; LaTourrette and Wasserburg, 1998; Hevey and Sanders, 2006; Qin et al., 2008; Harrison and Grimm, 2010; Henke et al., 2012; Monnereau et al., 2013; Gail and Trieloff, 2019), we calculated the evolution of the thermal profile within a chondrite parent body due to ^{26}Al heating. The size of the investigated body was assumed to be 80 km in radius, which is the approximate size of H and L chondrite parent bodies (e.g., Miyamoto et al., 1982; Bennett Iii and McSween Jr., 1996; Harrison and Grimm, 2010; Henke et al., 2012; Monnereau et al., 2013; Gail and Trieloff, 2019). The parent bodies of ECs were estimated to be comparable in size (Trieloff et al., 2022). Different sizes would lead to different thermal profiles at a given time, but they do not change much our conclusion regarding volatile loss from the most metamorphosed chondrites. The ^{26}Al/^{27}Al ratio at Solar System formation was $\sim 5 \times 10^{-5}$ (Russell et al., 1996; Huss et al., 2001). Assuming an Al concentration of 11.3 mg/g, corresponding to an H chondrite bulk composition (Wasson and Kallemeyn, 1988), the initial heat production of a planetesimal would be $\sim 1.9 \times 10^{-7}$ W kg^{-1} at Solar System formation or time zero (Qin et al., 2008). The maximum temperature attained within the body depends on the formation time of the body. Although it has been speculated that some chondrites might represent the outer, unmelted crust of a parent body with differentiated interior (Elkins-Tanton et al., 2011; Maurel et al., 2020), here we assume no significant melting at the center of the NC parent bodies by setting the formation time of the body to be 2 Myr after Solar System formation, corresponding to a maximum temperature at the center of the body of 1483 K.

Heat transport in the planetesimal happens through conduction (i.e., Fourier's law),

$$Q = -K\nabla T \tag{5}$$

where Q is the heat flux in W m^{-2}, K is the thermal conductivity in W m^{-1} K^{-1}, and ∇T is the thermal gradient in K m^{-1}. Considering energy balance, i.e., the total of the net energy flux and energy generated through radioactive decay of ^{26}Al must be balanced by the change in internal energy, Fourier's law leads to the heat production-transport equation in spherical coordinate,

$$\frac{dT}{dt} = \frac{1}{r^2}\frac{\partial}{\partial r}\left(r^2\kappa\frac{\partial T}{\partial r}\right) + \frac{\kappa H_0 \rho e^{-\lambda t}}{K} \tag{6}$$

where t is time in seconds after the formation of the planetary body, and r is the distance from the center in meter. H_0 is the initial heat production of ^{26}Al at the formation of the planetary body in W kg^{-1}. λ is the decay constant of ^{26}Al in s^{-1}. κ is the thermal diffusivity in m^2 s^{-1}, and is related to thermal conductivity K through $\kappa = \frac{K}{C_P \rho}$, where C_P is the specific heat capacity in the unit of J kg^{-1} K^{-1}, and ρ is the density in kg m^{-3}. For a first-order calculation, we assume that κ does not change, and Eq. (6) can be written as,

$$\frac{1}{\kappa}\frac{dT}{dt} = \frac{1}{r^2}\frac{\partial}{\partial r}\left(r^2\frac{\partial T}{\partial r}\right) + \frac{H_0 \rho e^{-\lambda t}}{K} \quad (7)$$

The analytical solution to Eq. (7) is (Carslaw and Jaeger, 1959),

$$T(r,t) = \frac{\kappa \rho H_0}{K\lambda} e^{-\lambda t}\left[\frac{a}{r}\frac{\sin r(\lambda/\kappa)^{1/2}}{\sin a(\lambda/\kappa)^{1/2}} - 1\right] + \frac{2a^3 \rho H_0}{r\pi^3 K}\sum_{n=1}^{\infty} \times \frac{(-1)^n}{n(n^2 - \lambda a^2/\kappa\pi^2)} \sin\frac{n\pi r}{a} e^{-\kappa n^2 \pi^2 t/a^2} \quad (8)$$

where a is the radius of the sphere. The values of the parameters used for the modelling are summarized in Table S3. The temperature profile as a function of time for a body of 80 km radius is shown in Fig. 11. Temperature is plotted against the distance to the center and the time after accretion (Fig. 11A). The temperature of the body first rises due to ^{26}Al heating, and then decreases due to heat conduction and loss at the surface. The center region reaches a higher maximum temperature than the outer region (Fig. 11B), and the maximum temperature (1483 K) is reached at the center about 10 Myr after its formation (Fig. 11C).

5.2.1.2. Evaporation thermodynamics. Equilibrium vapor pressure plays a central role in calculating the rate of evaporation in both kinetic and equilibrium regimes. Thermodynamic parameters relevant to evaporation of Rb and K from silicate melts (activity coefficient, evaporation coefficient, equilibrium constant) are relatively well constrained from laboratory experiments (Yu et al., 2003; Richter et al., 2011; Sossi et al., 2019; Zhang et al., 2021). These are however not applicable here as we are concerned with sub-solidus evaporation. In OCs, the main K host phase is sodium-rich plagioclase (oligoclase; Weirich et al., 2012). In ECs, K is hosted in several minerals including albitic plagioclase, roedderite (only in EH3-4), and djerfisherite (Kimura and Ikeda, 1998). Because the modal abundance of plagioclase (containing ~ 1 % K_2O) is about 10 times higher than roedderite (containing ~ 3 % K_2O) and djerfisherite (~9 % K) (Kimura and Ikeda, 1998), the amount of K in plagioclase and that in sulfide minerals of ECs are about equal. In this work, we do not consider evaporation of Rb and K from sulfide minerals, and we assume that the host mineral phase of K and Rb to be plagioclase. Thus, the modeling result is more applicable to OCs than ECs.

To model sub-solidus evaporation of K and Rb, we consider the following reaction between K-bearing plagioclase and olivine to form solid solution of orthopyroxene (Opx; Mg-Ts and En denote Al substituted Mg-Tschermak pyroxene and enstatite solid solution, respectively) and K gas (thermodynamics calculation suggests that the dominant K species in vapor is single atom K at the relevant conditions; Zhang et al., 2021; Dauphas et al., 2022),

$$KAlSi_3O_{8(s)} + 3\,Mg_2SiO_{4(S)} \rightleftarrows 0.5\,MgAl_2SiO_{6(S)} + 2.75\,Mg_2Si_2O_{6(S)} + K_{(g)} + 0.25O_{2(g)} [\text{Plagioclase} + \text{Olivine} \rightleftarrows \text{Opx solid solution (MgTs + En)} + K + O_2] \quad (9)$$

A similar reaction was assumed for Rb,

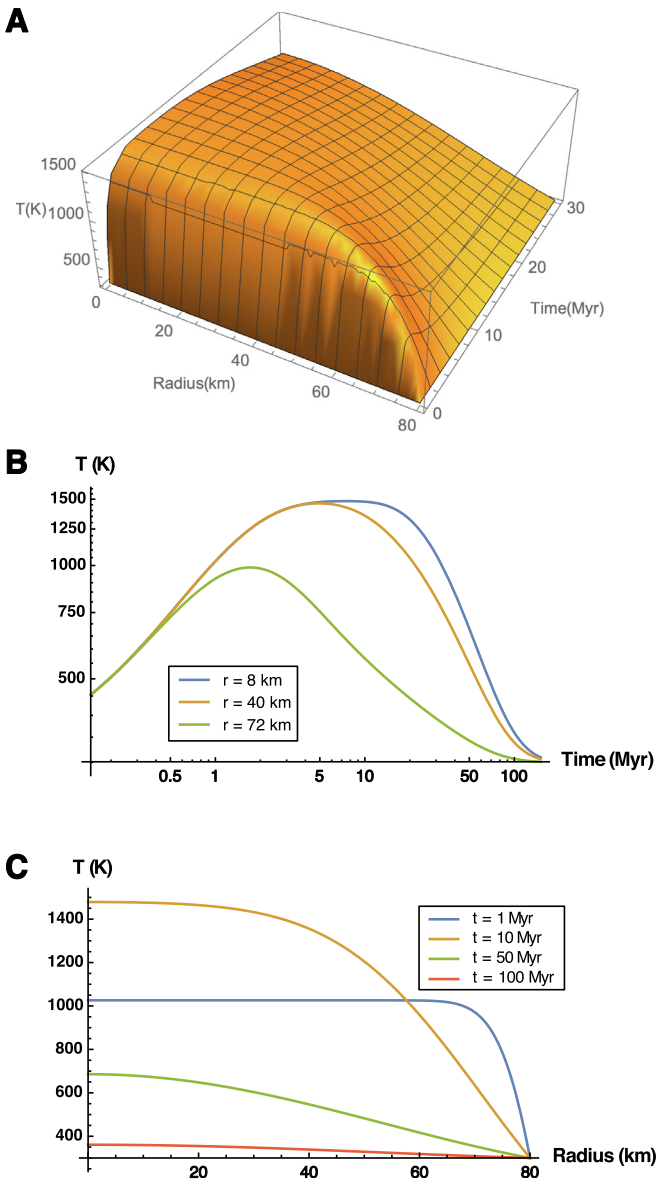

Fig. 11. Thermal evolution of an 80 km-radius chondrite parent body that formed 2 Myr after solar system formation (the maximum center temperature is 1483 K). (A) Temperature plotted as a function of distance to the center and time after the formation of the body. (B) Temperatures at 10 %, 50 %, and 90 % of the radius (i.e., 8 km, 40 km, and 72 km) plotted as a function of time. (C) Temperature profiles at different times (1Myr, 10 Myr, 50 Myr, and 100 Myr).

$$RbAlSi_3O_{8(s)} + 3\,Mg_2SiO_{4(S)} \rightleftarrows 0.5\,MgAl_2SiO_{6(S)} + 2.75\,Mg_2Si_2O_{6(S)} + Rb_{(g)} + 0.25O_{2(g)} \quad (10)$$

Equilibrium constants for the reactions above as a function of temperature were calculated using the thermodynamics data of phases in NIST-JANAF table (https://janaf.nist.gov/) and those reported by Berman (1988) and Holland and Powell (2011), using the equation $\ln K_{K,eq} = -\Delta G/RT$. The thermodynamics data (Gibbs free energy as a function of temperature) of $RbAlSiO_{4(s)}$ was not available and we calculated it by assuming that the Gibbs free energy of $RbAlSiO_{4(s)}$ minus that of $KAlSiO_{4(s)}$ is the same as the difference between the Gibbs free energy of $RbO_{0.5(s)}$ and $KO_{0.5(s)}$. The

polynomial fits of $K_{K,eq}$ and $K_{Rb,eq}$ as a function of temperature are (Table S3; to fit more precisely the fit was centered at the midpoint 1149.08 K of the temperature range from 298.15 to 2000 K),

$$\begin{aligned}\ln K_{K,eq} = &-33.6808 + 4.5319\times10^{-2}\times(T-1149.08)\\ &-3.8848\times10^{-5}\times(T-1149.08)^2+3.3762\\ &\times10^{-8}\times(T-1149.08)^3-2.9095\times10^{-11}\\ &\times(T-1149.08)^4+2.5669\times10^{-14}\\ &\times(T-1149.08)^5-3.0395\times10^{-17}\\ &\times(T-1149.08)^6+1.8564\times10^{-20}\\ &\times(T-1149.08)^7+8.1699\times10^{-23}\\ &\times(T-1149.08)^8+2.2381\times10^{-26}\\ &\times(T-1149.08)^9-6.5063\times10^{-28}\\ &\times(T-1149.08)^{10}-2.4949\times10^{-32}\\ &\times(T-1149.08)^{11}+2.2881\times10^{-33}\\ &\times(T-1149.08)^{12}+1.0294\times10^{-37}\\ &\times(T-1149.08)^{13}-4.6088\times10^{-39}\\ &\times(T-1149.08)^{14}-1.2346\times10^{-43}\\ &\times(T-1149.08)^{15}+4.7589\times10^{-45}\\ &\times(T-1149.08)^{16}+8.1424\times10^{-50}\\ &\times(T-1149.08)^{17}-1.9879\times10^{-51}\\ &\times(T-1149.08)^{18}\end{aligned} \tag{11}$$

$$\begin{aligned}\ln K_{Rb,eq} = &-32.6588 + 4.2862\times10^{-2}\times(T-1149.08)\\ &-3.7482\times10^{-5}\times(T-1149.08)^2+3.4923\\ &\times10^{-8}\times(T-1149.08)^3+1.8993\times10^{-11}\\ &\times(T-1149.08)^4-7.3307\times10^{-14}\\ &\times(T-1149.08)^5-6.1248\times10^{-16}\\ &\times(T-1149.08)^6+1.0373\times10^{-18}\\ &\times(T-1149.08)^7+3.4890\times10^{-21}\\ &\times(T-1149.08)^8-4.6056\times10^{-24}\\ &\times(T-1149.08)^9-1.1585\times10^{-26}\\ &\times(T-1149.08)^{10}+1.0554\times10^{-29}\\ &\times(T-1149.08)^{11}+2.1528\times10^{-32}\\ &\times(T-1149.08)^{12}-1.18256\times10^{-35}\\ &\times(T-1149.08)^{13}-2.0995\times10^{-38}\\ &\times(T-1149.08)^{14}+5.1893\times10^{-42}\\ &\times(T-1149.08)^{15}+8.2732\times10^{-45}\\ &\times(T-1149.08)^{16}\end{aligned} \tag{12}$$

The equilibrium constants (K_{eq}) for the reactions could also be expressed as,

$$K_{K,eq} = \frac{P_{K,eq}\,(P_{O_2})^{0.25}\,(a_{MgAl_2SiO_6})^{0.5}\,(a_{Mg_2Si_2O_6})^{2.75}}{(a_{Mg_2SiO_4})^3\,a_{KAlSi_3O_8}} \tag{13}$$

$$K_{Rb,eq} = \frac{P_{Rb,eq}\,(P_{O_2})^{0.25}\,(a_{MgAl_2SiO_6})^{0.5}\,(a_{Mg_2Si_2O_6})^{2.75}}{(a_{Mg_2SiO_4})^3\,a_{RbAlSi_3O_8}} \tag{14}$$

where P is partial vapor pressure, a is activity and equals the product of activity coefficient and mole fraction. Opx solid solution $[(Fe,Mg)^{M2}(Fe,Mg,Al)^{M1}(Al,Si)_2O_6]$ has six possible components, $Fe_2Si_2O_6$, $FeMgSi_2O_6$, $FeAl_2SiO_6$, $MgFeSi_2O_6$, $Mg_2Si_2O_6$, and $MgAl_2SiO_6$. The mole fractions of components Mg-Ts ($MgAl_2SiO_{6(S)}$) and En ($Mg_2Si_2O_{6(S)}$) in this study are estimated based on the chemical composition of Opx ($Fe_{0.43}Mg_{1.53}Al_{0.01}Si_{1.99}O_6$; Slater-Reynolds and McSween, 2005) in type 6 OCs. Assuming that all Al in Opx is in Mg-Ts (some could be in Fe-Ts), we calculate a mole fraction of Mg-Ts in Opx of ~ 0.005. The mole fraction of En in Opx can be estimated based on the observed Fe/Mg ratio ($Fe_{0.43}Mg_{1.53}$) in Opx, which gives a mole fraction of En between 0.55 and 0.75, and we use a value of 0.65 hereafter. The $MgAl_2SiO_6$-$Mg_2Si_2O_6$ system was considered as ideal solid solution (Wood and Banno, 1973), thus, the activity coefficients of the Opx components are assumed to be 1. Olivine is assumed to be a pure phase and has an activity of 1. For plagioclase, the mole fractionation of $KAlSi_3O_8$ is calculated by assuming that $KAlSi_3O_8$ is dissolved in plagioclase ($NaAlSi_3O_8$ – $CaAl_2Si_2O_8$), and can be calculated as the K/(K + Na + Ca) ratio (mole/mole). Using the measured K, Na, and Ca abundances in plagioclase of OCs of low metamorphic grades (Lewis et al., 2022), the original mole fraction of $KAlSi_3O_8$ is calculated to be 0.02. Given that Rb substitutes for K, the original mole fraction of $RbAlSi_3O_8$ would be the mole fraction of $KAlSi_3O_8$ multiplied by the Rb/K ratio (mole/mole; Wasson and Kallemeyn, 1988) in OCs, which yields $0.02\times0.0017 = 3.4\times10^{-5}$. The activity coefficient of $KAlSi_3O_8$ (and $RbAlSi_3O_8$) was estimated to be 9.47 for a low-K plagioclase (Or < 8 %) (Ghiorso, 1984). Because the total amount of K and Rb in plagioclase is small, the mole fractions of Mg-Ts and En in Opx do not change much even if the reaction progresses to near complete K and Rb evaporation (the change is smaller than other errors), we can thus assume that the activities of Mg-Ts and En are constant. We thus have,

$$\begin{aligned}K_{K,eq} &= \frac{P_{K,eq}\,(P_{O_2})^{0.25}\,(0.005)^{0.5}\,(0.65)^{2.75}}{9.47\times0.02\times[K]/[K]_0}\\ &= 0.1142\,\frac{P_{K,eq}\,(P_{O_2})^{0.25}}{[K]/[K]_0}\end{aligned} \tag{15}$$

$$\begin{aligned}K_{Rb,eq} &= \frac{P_{Rb,eq}\,(P_{O_2})^{0.25}\,(0.005)^{0.5}\,(0.65)^{2.75}}{9.47\times3.4\times10^{-5}\times[Rb]/[Rb]_0}\\ &= 67.17\,\frac{P_{Rb,eq}\,(P_{O_2})^{0.25}}{[Rb]/[Rb]_0}\end{aligned} \tag{16}$$

where $[K]/[K]_0$ and $[Rb]/[Rb]_0$ denote the K and Rb contents in solids relative to the original contents. Equilibrium constants are usually calculated with pressures in bar, and here we convert the unit to SI unit Pa by dividing the partial pressures by 10^5, which translates into the following formulas for $P_{K,eq}$ and $P_{Rb,eq}$,

$$P_{K,eq} = \frac{10^{25/4}}{0.1142}\,\frac{K_{K,eq}}{P_{O_2}^{1/4}}\,\frac{[K]}{[K]_0} \tag{17}$$

$$P_{Rb,eq} = \frac{10^{25/4}}{67.17}\,\frac{K_{Rb,eq}}{P_{O_2}^{1/4}}\,\frac{[Rb]}{[Rb]_0} \tag{18}$$

One can see from the above equations that if the equilibrium constants of K and Rb are similar (which is the case in reality), then the amount of evaporated K and Rb would be different by a factor of 67.17/0.1142 = 588 (mole/mole), which is the concentration difference between K and Rb in solids. As expected, the evaporation

process will lead to the same relative amount of evaporated K and Rb. In order to calculate $P_{K,eq}$, both the oxygen fugacity P_{O_2} and the equilibrium constant must be set. We assume the oxygen fugacity stays constant at IW − 1 (the oxygen fugacity of OCs is around IW − 1 while that of ECs is lower, around IW − 3; Larimer and Buseck, 1974; Brett and Sato, 1984). The effect of the oxygen fugacity on K and Rb evaporation is small due to the power 1/4 scaling.

5.2.1.3. Modeling evaporation and transport of Rb and K in chondrite parent bodies. The evaporation and gas transport process can be evaporation-limited or transport-limited. If it is transport-limited, an immediate chemical equilibrium between gas and solid during evaporation can be assumed, and the vapor pressure of the gas can be calculated conveniently as the equilibrium vapor pressure. If it is evaporation-limited, the vapor would be highly undersaturated and the process would be comparable to vacuum evaporation, which will lead to large volatile loss and isotopic fractionation.

The rate of evaporation is given by the Hertz-Knudsen equation,

$$J_i = \frac{\gamma_i (P_{i,eq} - P_i)}{\sqrt{2\pi M_i RT}} \tag{19}$$

where J_i is the evaporative flux of species i in mol m^{-2} s^{-1}, γ_i is evaporation coefficient of i, P_{eq} and P are equilibrium and instantaneous vapor pressures in Pa, M_i is molar mass of i in kg mol^{-1}, R is the gas constant (8.314 J mol^{-1} K^{-1}), and T is temperature in K. Converting the flux to mole flux,

$$dn_i = \frac{\gamma_i (P_{i,eq} - P_i)}{\sqrt{2\pi M_i RT}} S dt \tag{20}$$

where n_i is the moles of i in the evaporated gas, S is the surface area for evaporation, and t is time in s. Applying the ideal gas law ($P_i = \frac{n_i RT}{\varphi V}$, where V is the volume of the considered material and φ is the porosity), Eq. (20) can be solved as,

$$\frac{n_i}{n_{i,eq}} = 1 - \exp\left(-\frac{\gamma_i S}{\varphi V}\sqrt{\frac{RT}{2\pi M_i}}t\right) \tag{21}$$

The characteristic timescale for evaporation, if defined as ~ 63 % evaporation (i.e., 1–1/e), can be written as,

$$\tau_{i,ev} = \frac{\varphi V}{\gamma_i S}\sqrt{\frac{2\pi M_i}{RT}} \tag{22}$$

The migration of gas within a body follows Darcy's law, that is, the instantaneous flux is proportional to the pressure gradient,

$$q_i = -\frac{\xi}{\mu}\frac{\partial P_i}{\partial r} \tag{23}$$

where q_i is the instantaneous gas flux of i in m s^{-1}, ξ the permeability in m^2, μ the dynamic viscosity in Pa s and $\partial P/\partial r$ the pressure gradient. The characteristic timescale for gas transport across the planetesimal ($\tau_{i,tr}$) can be approximated as $a/|q_i|$, with a the planetesimal radius,

$$\tau_{i,tr} = \frac{a^2 \mu}{P_{i,eq}\xi} \tag{24}$$

From the two timescales for evaporation and transport [Eqs. (23) and (14)], we can calculate the dimensionless Damköhler number, which is the ratio of flow timescale to chemical reaction timescale,

$$Da = \tau_{i,tr}/\tau_{i,ev} = \frac{a^2 \mu}{P_{i,eq}\xi}\frac{\gamma_i S}{\varphi V}\sqrt{\frac{RT}{2\pi M_i}} \tag{25}$$

$Da \gg 1$ means that volatile loss is transport-limited, while $Da \ll 1$ means that volatile loss is evaporation-limited. We have calculated Da at the maximum center temperature of 1483 K. For an assumed body sized $a = 80$ km, we obtain a value of Da of $\sim 10^{20}$, meaning that K and Rb volatile loss during metamorphism on the parent-body(ies) of ordinary (and possibly enstatite) chondrites would be transport-limited. Practically, this means that despite the outward permeable transport, evaporation was fast enough compared to the transport to maintain the vapor in the pore spaces in a state of near equilibrium with the solid residue. Outward transport happened primarily through the equilibrium vapor pressure gradient established radially due to the large temperature gradient present in the planetesimal between its interior and the surface (Fig. 11).

To simulate the volatilization and gas transport process, we solved Eq. (23) using a finite difference approach, and the pressure term in the equation was assumed to be equilibrium vapor pressure [Eqs. (15) and (16)]. The planetesimal was divided radially into 2000 layers of equal volume (equal number of atoms). We did not use equal width for each layer because the resolution was insufficient to treat transport near the surface. Time was divided into discrete intervals of 1 Myr durations and we tracked the evolution of the body for 100 My. For each time interval, we first calculated the temperature profile within the body [Eq. (8)] at that time. Equilibrium evaporation from the solid was assumed and the equilibrium vapor pressure of K or Rb was calculated according to Eq. 17 or 18. We then calculated the flux across each layer, driven by the equilibrium vapor pressure gradient [Eq. (23)] for that time interval. If the vapor pressure of the element after gas migration exceeded the equilibrium vapor pressure at the temperature at the end of that time interval, condensation was assumed and atoms were transferred from the vapor to the solid to allow a new chemical equilibrium to be reached. Conversely, if the vapor pressure of the element after gas migration was lower than the equilibrium vapor pressure at that temperature, evaporation was assumed, and atoms were transferred from the solid to the vapor to allow a new chemical equilibrium. This procedure was iterated until 100 Myr. We assumed a spherically symmetric body and imposed a no-flux boundary condition at the center. The temperature at the surface of the planetesimal was always cold enough (300 K) as to act as a cold trap that would prevent K and Rb from escaping the planetesimal. We ran the numerical code with different total number of layers and time interval durations and such sensitivity tests had negligible impact on the results.

The main output of the model is the flux (in, out, and net flux, in unit of moles) of each layer at each time. In Fig. 12, the gas fluxes are plotted as a function of radius. The possible original locations of the meteorites (type 3 to type 6) are also labeled. For determining these locations, the following maximum metamorphic temperatures were assumed (Dodd, 1981; McSween Jr et al., 1988; Bennett Iii and McSween Jr., 1996): $T_{max} \leq 873$ K (type 3), 873 K < $T_{max} \leq$ 973 K (type 4), 973 K < $T_{max} \leq$ 1023 K (type 5), and 1023 K < $T_{max} \leq$ 1300 K (type 6). The corresponding locations were found to be: R ≥ 74 km (type 3), 72.3 km ≤ R < 74 km (type 4), 71.3 km ≤ R < 72.3 km (type 5), and 62.5 km ≤ R < 71.3 km (type 6). Some earlier work assumed the location of type 6 OCs extending to the center of the parent body (e.g., Miyamoto et al., 1982; Bennett Iii and McSween Jr., 1996) but it is likely that deeper samples with higher metamorphic temperature are missing from our current meteorite collection (e.g., Henke et al., 2012; Trieloff et al., 2022).

The results show migration of Rb and K from the center (negative net flux) of the body towards the surface, and condensation near the surface (positive net flux) (Fig. 12A and B). The net fluxes were integrated over the 100 Myr thermal evolution, by then all

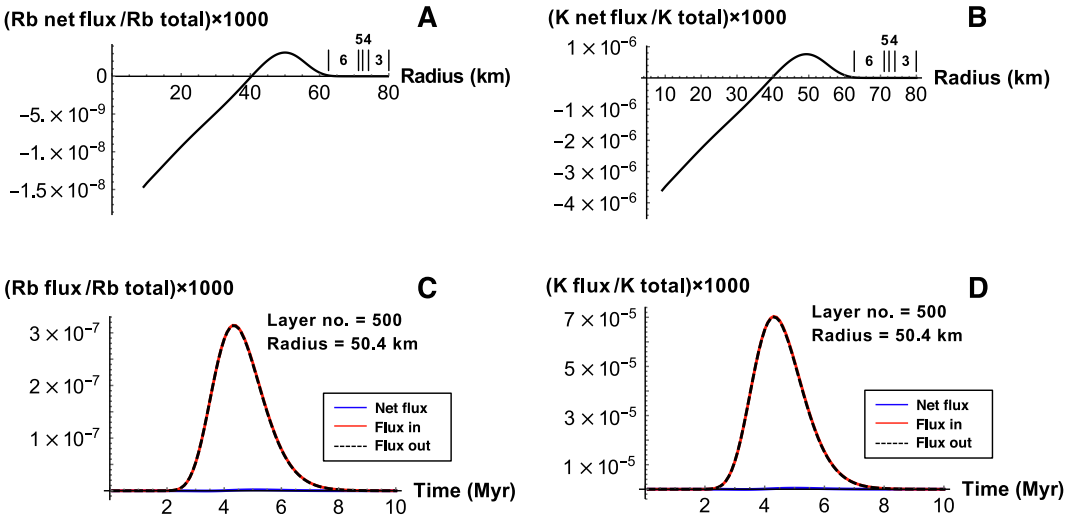

Fig. 12. The migration of gaseous Rb and K inside a chondrite parent body (80 km radius) due to volatilization and gas transport during parent-body thermal metamorphism. For modeling, the body was divided into 2000 layers of equal volume (decreasing width from the center to the surface). Shown are the net flux in (flux in minus flux out) of Rb and K within individual layers (panels A and B) after 100 Myr thermal evolution of the body due to ^{26}Al decay. The Rb or K flux of each layer was normalized to the total amount of Rb or K within the layer, and multiplied by a factor of 1000. Numbers 3, 4, 5, 6 denote the possible locations of type 3, 4, 5, and 6 meteorites. Panels C and D show the flux in, flux out, and net flux of an arbitrary layer no. 500, corresponding to a distance to the center of 50.4 km. The results show that the amount of Rb and K transport is negligible, and the process cannot produce observable isotopic fractionation.

^{26}Al would have decayed and the temperature of the body would have decreased to the ambient temperature (assumed to be 300 K). The net fluxes of Rb and K were calculated for each layer, and were normalized to the total number of Rb and K atoms within the layer, and then a factor of 1000 was multiplied (considering that isotopic fractionations are usually measured at per mil level). Fig. 12C and D show the Rb and K gas fluxes in the 500th layer (radius at 50.4 km). Overall, the calculated fluxes are all very small, suggesting that the amount of gas transport is negligible, and the associated isotope fractionation should be negligible. More reducing environment (relevant to ECs) would enhance evaporation, but the effect of oxygen fugacity is rather limited because the equilibrium constant is proportional to oxygen fugacity to the power of ¼ [Eqs. (15) and (16)]. Our tests suggest that by decreasing oxygen fugacity from IW − 1 to IW − 4 that is relevant to ECs, the net transport amount only increases by a factor of ∼ 30. The relative amount of transported K is higher than that of Rb, this is because although evaporation would produce moles of Rb and K in the gas proportional to their concentrations in the solid [i.e., a factor of $\frac{67.17}{0.1142} = 588$ (mole/mole) difference; Eqs. (17) and (18); assuming their equilibrium constants are similar], the moles of transported gas ($n_{i,\mathrm{tr}}$) is proportional to the square of the vapor pressure ($n_{i,\mathrm{tr}} = q_i A \rho_i = -\frac{\xi}{\mu}\frac{P_{i,\mathrm{eq}}}{r}\frac{P_{i,\mathrm{eq}} M_i}{RT} A$, where ρ_i is the gas density and A is surface area for gas transport). Comparing the equilibrium constants of Rb and K [Eqs. (11) and (12)] shows that Rb is slightly more volatile than K, but this cannot compensate the difference in transport efficiency between the two elements.

To summarize, the calculation above shows that evaporation and gas transport during thermal metamorphism of chondrite parent bodies cannot lead to significant migration of K and Rb, at least for the conditions assumed above (dry evaporation through plagioclase decomposition; the effect of water or fluids was not considered), and therefore cannot cause observable isotopic fractionation. The main reasons for this are, (i) the metamorphic temperature is too low (sub-solidus evaporation) to cause large amount of volatilization of the two elements from solids (the evaporation amount is too small compared to the amount in the solids), and (ii) the process is gas transport-limited and the transport is inefficient.

5.2.2. Diffusion-driven isotopic fractionation during parent-body metamorphism

In the calculation above we did not consider diffusion between minerals during parent-body metamorphism. Alkalis could diffuse from high to low concentration regions at the hand specimen scale at elevated temperatures, causing large kinetic isotopic fractionation (Richter et al., 2003, 2009). Chondrites accreted from materials with heterogeneous alkali element contents. Without metamorphic equilibration, regions with distinct K and Rb concentrations and similar isotopic compositions could coexist. As chondrite parent bodies experience heating during metamorphism, those chemical differences can be erased by diffusion, which we expect to be accompanied by isotopic fractionation driven by the fact that light isotopes diffuse faster than heavier ones. The K, Rb-rich regions that export those elements acquire high δ^{87}Rb and δ^{41}K values, while K, Rb-poor regions that receive those elements acquire low δ^{87}Rb and δ^{41}K values. Those fractionations are however transient, as they are finally erased if the two regions are fully equilibrated at the metamorphic temperature. The K isotopic compositions of higher metamorphic grade OCs and ECs seem to show larger isotopic dispersion encompassing those of the low metamorphic grade ones (Fig. 6D and E), which is consistent with a diffusion-mediated isotopic fractionation during partial re-equilibration. The Rb isotopic variations do not show this pattern (i.e., the values of higher metamorphic grade samples do not encompass those of low metamorphic grade ones) but seem to be shifted to higher values in higher metamorphic grade samples (Figs. 4 and 5), which could be due to the small number of Rb samples (sampling bias) or other processes besides diffusion.

Here we do a simple calculation to check whether diffusion could cause measurable isotopic variation at the hand specimen scale. There are two types of diffusion (Dohmen and Milke, 2010; Zhang, 2010), volume diffusion occurring inside a mineral phase and grain boundary diffusion (diffusion along grain boundaries).

Grain boundary diffusion is several orders of magnitude faster than volume diffusion, and could cause elemental and isotopic fractionations at large spatial scales (e.g., Teng et al., 2006; Kuhnel et al., 2021). The diffusion rates of K within feldspar and along grain boundaries of feldspar aggregates have been studied experimentally. We use these rates to estimate the isotopic fractionation associated with diffusion during thermal metamorphism of NC parent bodies.

The K diffusion coefficient for grain boundary diffusion (D_{gb}) in fine-grained feldspar aggregates as a function of temperature can be expressed as (calculated using the Arrhenius parameters in Farver and Yund (1995a),

$$D_{gb} = \frac{e^{-24655.83/T}}{2.5 \times 10^{10} d_{gb}} \quad (26)$$

where T is temperature in Kelvin, D_{gb} is the grain boundary diffusion coefficient in $m^2\ s^{-1}$, and d_{gb} is the effective grain boundary width in m. The K diffusion coefficient for volume diffusion (D_v; in $m^2\ s^{-1}$) can be expressed, using the Arrhenius parameters in Foland et al. (1974), as,

$$D_v = 0.00161 e^{-34294.96/T} \quad (27)$$

The bulk diffusivity can be determined by the relative contributions of volume and grain boundary diffusion (Farver and Yund, 1995b),

$$D_{bulk} = D_v + \frac{\pi d_{gb}}{d_g} D_{gb} \quad (28)$$

where d_g is the grain size in m, and $\frac{\pi d_{gb}}{d_g}$ calculates the fractional area occupied by grain boundaries assuming a spherical grain geometry. Using a typical grain size d_g of 1 mm, an effective grain boundary width d_{gb} of 1 nm, and a metamorphic temperature of 1000 K, the bulk diffusivity of K is calculated to be 4.52×10^{-18} $m^2\ s^{-1}$, with about equal contributions from volume and grain boundary diffusion. For calculating the isotopic effect, the diffusivities of both ^{41}K and ^{39}K are required. The diffusivity above is more akin to ^{41}K, given that ^{41}K was used as the tracer isotope in those experiments. For calculating the diffusivity of ^{39}K, we use the assumption that the ratio of the diffusivities of two isotopes is related to their masses through a beta factor (β) (Richter et al., 2003),

$$\frac{D_{39K,bulk}}{D_{41K,bulk}} = \left(\frac{M_{41K}}{M_{39K}}\right)^{\beta} \quad (29)$$

where $D_{39K,bulk}$ and $D_{41K,bulk}$ are the bulk diffusivities of ^{39}K and ^{41}K, respectively, and M_{41K} and M_{39K} are the masses of the two isotopes. The β value is 0.5 for ideal gases, and < 0.5 in other cases. The β value for different element could be different. Richter et al. (2003) determined a β value of 0.215 for Li diffusion in silicate melts and 0.075 for Ca diffusion. The β value for K in basaltic melts was constrained to be ~ 0.07, similar to Li (Zhang et al., 2021), and we use this value to calculate the bulk diffusivity of ^{39}K.

The concentration of each isotope during diffusion as a function of its diffusivity and the diffusion time and distance can be described using the solution to the Fick's law of diffusion (Crank, 1979). If we consider a one-dimensional low K concentration (K-depleted) area of width $2l$ in contact with K-enriched area on each side and a total width of $2L$ (K-depleted + K-enriched area), the concentration profile solved from the diffusion equation using a no-flux boundary condition is,

$$\frac{c_{x,t} - c_1}{c_0 - c_1} = \frac{L - l}{L} - \sum_{n=1}^{\infty} \frac{2 \sin\left(\frac{n\pi l}{L}\right) \cos\left(\frac{n\pi x}{L}\right) \exp\left[-\left(\frac{n\pi}{L}\right)^2 D_{bulk} t\right]}{n\pi} \quad (30)$$

where $c_{x,t}$ is the K concentration at distance x to the center of the depleted area, c_0 and c_1 are the initial K concentrations in the K-enriched area and the K-depleted area, respectively, and t is time. For calculation, we were interested in the hand specimen scale, thus assumed $2l$ to be 10 cm. We assumed $c_1/c_0 = 0.4$, similar to the observed concentration variation in NCs. The bulk diffusivities of ^{41}K and ^{39}K, calculated using Eqs. (26)–(29) assuming a constant temperature of 1000 K and a β value of 0.07, are 4.5167×10^{-18} $m^2\ s^{-1}$ and 4.5325×10^{-18} $m^2\ s^{-1}$, respectively. Taking $L = 2l$ (i.e., the K-depleted and K-enriched area are of the same size), the concentration $c_{x,t}$ relative to c_0 is plotted as a function of the distance x for various time durations of diffusion (t = 0.1 Myr, 1Myr, 5Myr, 10 Myr, 15Myr, and 20 Myr) in Fig. 13A. The isotopic profiles are plotted in Fig. 13B. We also plot the bulk K isotopic compositions of the K-enriched and K-depleted areas as a function of diffusion time (Fig. 13C), and the isotopic difference between the two areas as a function of their concentration difference (Fig. 13D). Overall, the K isotopic variation calculated from the modeling ranges about 1 ‰, which is comparable to the observed K isotopic variations in NC samples. The Rb diffusion is more difficult to constrain because the lack of the grain boundary diffusion data. For volume diffusion the Rb diffusion rate is smaller than K (Foland et al., 1974; Giletti and Shanahan, 1997), but it is unknown if this is the case for grain boundary diffusion. For major elements in grain boundary diffusion, it can be safely assumed that their concentrations in grain boundaries are similar to their concentrations in mineral grains, but for trace elements (especially incompatible elements) they could have enhanced segregation in grain boundaries so that their diffusivities are enhanced. The segregation factors of trace elements like Rb require further study. Nonetheless, the calculation shows that diffusion during thermal metamorphism of NC parent bodies is a viable mechanism for explaining the observed K isotopic variation in NCs.

5.3. Shock heating during impacts

Shock heating/metamorphism can potentially affect the chemical composition of meteorites, as has been documented for Te, Zn, and Cd, which seem to be more depleted in strongly shocked L chondrites compared to mildly shocked L chondrites (Friedrich et al., 2004), possibly because of massive impact(s) on the parent body that happened ~ 500 Myr ago (Bogard et al., 1976; Bogard and Hirsch, 1980). We find however no clear correlation between shock levels and either $\delta^{41}K$ or $\delta^{87}Rb$ (Figs. 4 and 5). In OC samples, the more heavily shocked samples seem to have Rb isotopic compositions that extend to heavier values (Fig. 5A), but a trend is not clear. The EC samples have shock levels of S2–4 (Table S1 and Fig. 4). Abee (EH4) has a shock level of S2–4 and is plotted as S2 in Fig. 4. If S4 is more appropriate, a weak trend emerges between Rb isotopic compositions and shock levels (Fig. 4A). If real, the more heavily shocked samples have lighter Rb isotopic compositions, which is the opposite of what one would expect for evaporative volatile loss during shock heating. A caveat, however, is that some high petrologic type NCs have experienced shocks that were later overprinted by thermal metamorphism (e.g., type 5 and 6 metamorphism can repair damage from S5 shocks), especially in ECs which suffered more shock damage than OCs and CCs (Rubin et al., 1997). Thus, the current shock levels might not represent the entire shock history the samples experienced.

There is evidence that impacts have induced Rb migration and isotopic fractionation. Previous Rb-Sr isochron studies of whole rock L chondrites found disturbed Rb-Sr system that is consistent with Rb volatilization due to impact reheating (Minster and Allégre, 1979). Shocks have also affected the Rb-Sr in EC rocks

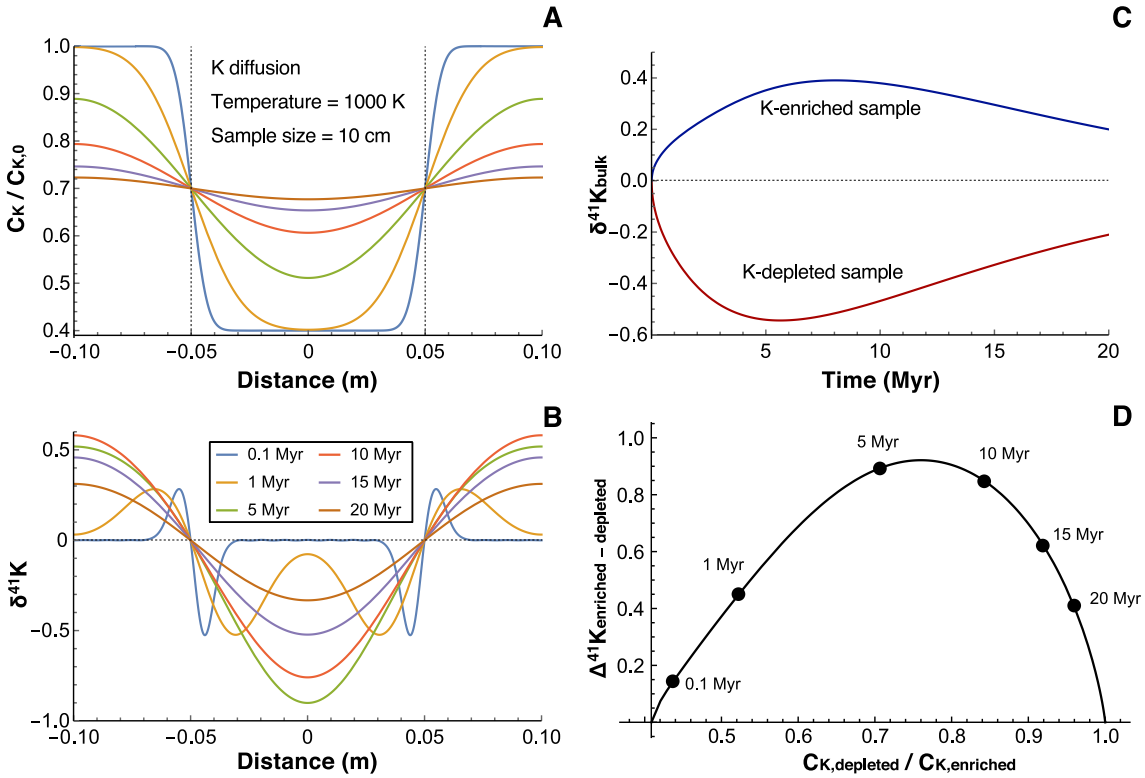

Fig. 13. Modeling of diffusion-caused K re-distribution and isotopic fractionation during NC parent-body metamorphism. The model assumes a K-depleted area/sample (10 cm in width) in contact with K-enriched areas on both sides. The metamorphic temperature is assumed to be 1000 K. The original K concentration in the K-depleted area is assumed to be 40 % of that of the K-enriched area. (A) K concentration profiles calculated for various diffusion times (0.1 Myr, 1 Myr, 5 Myr, 10 Myr, 15 Myr, and 20 Myr). (B) K isotopic composition profiles. (C) The bulk K isotopic compositions of the K-enriched area (labelled as "K-enriched sample") and the K-depleted area (labelled as "K-depleted sample") as a function of diffusion time. (D) The isotopic difference between the K-enriched sample and the K-depleted sample as a function of their concentration difference (the K concentration in the K-depleted sample divided by that of the K-enriched sample). As time (labelled on the curve) proceeds, the elemental difference becomes smaller, while the isotopic difference first becomes larger due to kinetic diffusion, then becomes smaller and eventually reach equilibrium. Potassium isotope fractionation by diffusion during parent-body thermal metamorphism could explain the observed K isotopic variation in NCs.

and minerals (Minster et al., 1979). Although impact heating is transient compared to parent-body thermal metamorphism, impacts would affect samples that are near the surface, and the volatilized species from these samples could escape to space more efficiently. Thus, some of the Rb isotopic variations in NCs could be due to impact heating and volatilization. Potassium is probably less affected by this process because it is less volatile than rubidium. Future work is needed to study how much Rb and K isotopic fractionations in NCs could be induced by impact heating.

6. Conclusions

1. We measured Rb and K isotopic compositions of NCs (OCs and ECs) and Martian meteorites (Table 1). The NCs, OCs in particular, show much larger isotopic variations than CCs or samples from differentiated bodies (Fig. 1).
2. We constrained the bulk Rb and K isotopic compositions of planetary bodies (Table 1). The bulk Rb isotopic composition of Mars was constrained to be +0.10 ± 0.03 ‰ using the correlation between δ^{87}Rb and La/U ratio (Fig. 3), and the bulk K isotopic composition was constrained to be −0.26 ± 0.05 ‰ by averaging over data from this study and the literature. The bulk Moon is +0.03 ± 0.03 ‰ for Rb and −0.01 ± 0.02 ‰ for K, and the Earth is −0.13 ± 0.01 ‰ for Rb and −0.44 ± 0.02 ‰ for K. We used kernel density estimates (KDEs) to constrain the Rb and K isotopic compositions of bulk OC and EC parent bodies (Fig. 6), and the values are: OC $-0.12^{+0.15}_{-0.24}$‰ for Rb and $-0.72^{+0.28}_{-0.41}$ ‰ for K, EC $+0.02^{+0.29}_{-0.26}$ ‰ for Rb and $-0.33^{+0.37}_{-0.23}$‰ for K. The bulk K isotopic compositions of subgroup OCs were estimated using KDEs to be H $-0.72^{+0.26}_{-0.55}$ ‰, L $-0.71^{+0.23}_{-0.39}$ ‰, and LL $-0.77^{+0.63}_{-0.30}$ ‰.
3. The Rb and K isotopic compositions of bulk planetary bodies show a broad correlation (Fig. 8), suggesting that the δ^{87}Rb and δ^{41}K isotopic variations reflect a volatility control, and are not nucleosynthetic anomalies. Individual samples show isotopic dispersion in the Rb vs K plot (Fig. 2). Samples with higher metamorphic grades plot off the elemental and isotopic trends, suggesting that chondrite parent-body processes (most likely thermal diffusion and impact evaporation) have fractionated the two isotopic systems.
4. We calculated whether heterogeneity in chondrule isotopic composition (chondrule "nugget effect") could explain the observed Rb and K isotopic variations in individual NC samples. Our modeling shows that the process could induce isotopic variations of ~±0.25 ‰ for K and ±0.13 ‰ for Rb when sampling mass is 200 mg, which are not sufficient to explain the observed isotopic variations. For overcoming this chondrule "nugget effect" and obtaining a more representative isotopic composition, sample masses at the gram level are preferred in future studies (Fig. 9).
5. We modeled volatilization of elements and transport of them during parent-body thermal metamorphism to test whether it could account for the observed Rb and K isotopic variations in NC samples. The process is transport-limited and is inefficient in transporting MVEs and causing isotopic fractionation (Fig. 12). In contrast, thermal diffusion during parent-body

metamorphism could lead to K isotopic variation comparable to the observed variation. Other processes such as fluid alteration and shock vaporization might have also played a role in modifying the original isotopic compositions.

Declaration of Competing Interest

The authors declare that they have no known competing financial interests or personal relationships that could have appeared to influence the work reported in this paper.

Acknowledgments

The work was supported by a NASA NESSF fellowship (NNX15AQ97H) to NXN, NASA grants NNX17AE86G (LARS), 80NSSC17K0744 (HW), 000306-002 (HW), 80NSSC21K0380 (EW), 0995GXB174 (EW), NSF grant EAR-2001098 (CSEDI), and funding from DOE to ND. NXN was partially supported by a Packard Fellowship to FLHT.

Appendix A. Supplementary material

The supplementary material contains supplementary tables S1, S2, and S3. Table S1 shows the shock levels of the NC samples. Table S2 compiles K, Rb, Te, and Zn isotopic compositions of NCs from this study and literature. Table S3 gives the values of the parameters that were used for modeling chondrite parent body thermal metamorphism.

Supplementary material to this article can be found online at https://doi.org/10.1016/j.gca.2023.01.004.

References

Alexander, C.M.O., 2019. Quantitative models for the elemental and isotopic fractionations in chondrites: The carbonaceous chondrites. Geochim. Cosmochim. Acta 254, 277–309.
Alexander, C.M.O., Grossman, J.N., 2005. Alkali elemental and potassium isotopic compositions of Semarkona chondrules. Meteorit. Planet. Sci. 40, 541–556.
Alexander, C.M.O., Grossman, J.N., Wang, J., Zanda, B., Bourot-Denise, M., Hewins, R. H., 2000. The lack of potassium-isotopic fractionation in Bishunpur chondrules. Meteorit. Planet. Sci. 35, 859–868.
Balta, J.B., Sanborn, M.E., Udry, A., Wadhwa, M., McSween Jr., H.Y., 2015. Petrology and trace element geochemistry of Tissint, the newest shergottite fall. Meteorit. Planet. Sci. 50, 63–85.
Bennett Iii, M. E. and McSween, Jr. H. Y. (1996) Revised model calculations for the thermal histories of ordinary chondrite parent bodies. Meteorit. Planet. Sci. 31, 783–792.
Berman, R.G., 1988. Internally-consistent thermodynamic data for minerals in the system Na_2O-K_2O-CaO-MgO-FeO-Fe_2O_3-Al_2O_3-SiO_2-TiO_2-H_2O-CO_2. J. Petrol. 29, 445–522.
Bischoff, A., Schleiting, M., Wieler, R., Patzek, M., 2018. Brecciation among 2280 ordinary chondrites – Constraints on the evolution of their parent bodies. Geochim. Cosmochim. Acta 238, 516–541.
Bloom H., Lodders K., Chen H., Zhao C., Tian Z., Koefoed P., Pető M. K., Jiang Y. and Wang (王昆) K. 2020. Potassium isotope compositions of carbonaceous and ordinary chondrites: Implications on the origin of volatile depletion in the early solar system. Geochim. Cosmochim. Acta 277, 111–131.
Bogard, D.D., Hirsch, W.C., 1980. ^{40}Ar-^{39}Ar dating, Ar diffusion properties, and cooling rate determinations of severely shocked chondrites. Geochim. Cosmochim. Acta 44, 1667–1682.
Bogard, D.D., Husain, L., Wright, R.J., 1976. ^{40}Ar-^{39}Ar dating of collisional events in chondrite parent bodies. J. Geophys. Res. 1896–1977 (81), 5664–5678.
Brasser, R., Dauphas, N., Mojzsis, S.J., 2018. Jupiter's influence on the building blocks of Mars and Earth. Geophys. Res. Lett. 45, 5908–5917.
Braukmüller, N., Wombacher, F., Funk, C., Münker, C., 2019. Earth's volatile element depletion pattern inherited from a carbonaceous chondrite-like source. Nat. Geosci. 12, 564–568.
Brett, R., Sato, M., 1984. Intrinsic oxygen fugacity measurements on seven chondrites, a pallasite, and a tektite and the redox state of meteorite parent bodies. Geochim. Cosmochim. Acta 48, 111–120.
Britt, D.T., Pieters, C.M., 1991. Black ordinary chondrites: An analysis of abundance and fall frequency. Meteoritics 26, 279–285.
Burkhardt, C., Spitzer, F., Morbidelli, A., Budde, G., Render, J.H., Kruijer, T.S., Kleine, T., 2021. Terrestrial planet formation from lost inner solar system material. Sci. Adv. 7, eabj7601.
Carslaw, H., Jaeger, J., 1959. Heat Conduction in Solids. Oxford University Press.
Chen, H., Tian, Z., Tuller-Ross, B., Korotev, R.L., Wang, K., 2019. High-precision potassium isotopic analysis by MC-ICP-MS: an inter-laboratory comparison and refined K atomic weight. J. Anal. At. Spectrom. 34, 160–171.
Chen, H., Saunders, N.J., Jerram, M., Halliday, A.N., 2021. High-precision potassium isotopic measurements by collision cell equipped MC-ICPMS. Chem. Geol., 120281.
Clayton, R.N., 1993. Oxygen isotopes in meteorites. Annu. Rev. Earth Planet. Sci. 21, 115–149.
Crank, J., 1979. The Mathematics of Diffusion. Oxford University Press.
Dauphas, N., 2017. The isotopic nature of the Earth's accreting material through time. Nature 541, 521–524.
Dauphas, N., Poitrasson, F., Burkhardt, C., Kobayashi, H., Kurosawa, K., 2015. Planetary and meteoritic Mg/Si and δ^{30}Si variations inherited from solar nebula chemistry. Earth Planet. Sci. Lett. 427, 236–248.
Dauphas, N., Nie, N.X., Blanchard, M., Zhang, Z.J., Zeng, H., Hu, J.Y., Meheut, M., Visscher, C., Canup, R., Hopp, T., 2022. The extent, nature, and origin of K and Rb depletions and isotopic fractionations in Earth, the Moon, and other planetary bodies. Planet. Sci. J. 3, 29.
Dauphas, N., Pourmand, A., 2015. Thulium anomalies and rare earth element patterns in meteorites and Earth: Nebular fractionation and the nugget effect. Geochim. Cosmochim. Acta 163, 234–261.
Dauphas, N., Schauble, E.A., 2016. Mass fractionation laws, mass-independent effects, and isotopic anomalies. Annu. Rev. Earth Planet. Sci. 44, 709–783.
Davis, A.M., 2006. Volatile evolution and loss. Meteorites and the early solar system II 1, 295–307.
Dodd, R., 1969. Metamorphism of the ordinary chondrites: A review. Geochim. Cosmochim. Acta 33, 161–203.
Dodd, R.T., 1981. Meteorites: A Petrologic-Chemical Synthesis. Cambridge University Press.
Dohmen, R., Milke, R., 2010. Diffusion in polycrystalline materials: grain boundaries, mathematical models, and experimental data. Rev. Mineral. Geochem. 72, 921–970.
Elkins-Tanton, L.T., Weiss, B.P., Zuber, M.T., 2011. Chondrites as samples of differentiated planetesimals. Earth Planet. Sci. Lett. 305, 1–10.
Farver, J.R., Yund, R.A., 1995a. Grain boundary diffusion of oxygen, potassium and calcium in natural and hot-pressed feldspar aggregates. Contrib. Mineral. Petrol. 118, 340–355.
Farver, J.R., Yund, R.A., 1995b. Interphase boundary diffusion of oxygen and potassium in K-feldspar/quartz aggregates. Geochim. Cosmochim. Acta 59, 3697–3705.
Fehr, M.A., Hammond, S.J., Parkinson, I.J., 2018. Tellurium stable isotope fractionation in chondritic meteorites and some terrestrial samples. Geochim. Cosmochim. Acta 222, 17–33.
Fitoussi, C., Bourdon, B., Wang, X., 2016. The building blocks of Earth and Mars: A close genetic link. Earth Planet. Sci. Lett. 434, 151–160.
Foland, K.A., Hofmann, A.W., Giletti, B.J., Yoder, H.S., Yund, R.A., 1974. Alkali diffusion in orthoclase. Geochem. Transp. Kinet. 634, 77–98.
Friedrich, J.M., Bridges, J.C., Wang, M.-S., Lipschutz, M.E., 2004. Chemical studies of L chondrites. VI: variations with petrographic type and shock-loading among equilibrated falls. Geochim. Cosmochim. Acta 68, 2889–2904.
Friedrich, J.M., Ruzicka, A., Macke, R.J., Thostenson, J.O., Rudolph, R.A., Rivers, M.L., Ebel, D.S., 2017. Relationships among physical properties as indicators of high temperature deformation or post-shock thermal annealing in ordinary chondrites. Geochim. Cosmochim. Acta 203, 157–174.
Gail, H.-P., Trieloff, M., 2019. Thermal history modelling of the L chondrite parent body. Astron. Astrophys. 628, A77.
Ghiorso, M.S., 1984. Activity/composition relations in the ternary feldspars. Contrib. Mineral. Petrol. 87, 282–296.
Giletti, B.J., Shanahan, T.M., 1997. Alkali diffusion in plagioclase feldspar. Chem. Geol. 139, 3–20.
Grossman, J.N., Alexander, C.M.O., Wang, J., Brearley, A.J., 2000. Bleached chondrules: Evidence for widespread aqueous processes on the parent asteroids of ordinary chondrites. Meteorit. Planet. Sci. 35, 467–486.
Halliday, A.N., Porcelli, D., 2001. In search of lost planets – the paleocosmochemistry of the inner solar system. Earth Planet. Sci. Lett. 192, 545–559.
Harrison, K.P., Grimm, R.E., 2010. Thermal constraints on the early history of the H-chondrite parent body reconsidered. Geochim. Cosmochim. Acta 74, 5410–5423.
Hashizume, K., Sugiura, N., 1998. Transportation of gaseous elements and isotopes in a thermally evolving chondritic planetesimal. Meteorit. Planet. Sci. 33, 1181–1195.
Heier, K.S., Adams, J.A., 1964. The geochemistry of the alkali metals. Phys. Chem. Earth 5, 253–381.
Hellmann, J.L., Hopp, T., Burkhardt, C., Kleine, T., 2020. Origin of volatile element depletion among carbonaceous chondrites. Earth Planet. Sci. Lett. 549, 116508.
Hellmann, J.L., Hopp, T., Burkhardt, C., Becker, H., Fischer-Gödde, M., Kleine, T., 2021. Tellurium isotope cosmochemistry: Implications for volatile fractionation in chondrite parent bodies and origin of the late veneer. Geochim. Cosmochim. Acta 309, 313–328.
Henke, S., Gail, H.-P., Trieloff, M., Schwarz, W.H., Kleine, T., 2012. Thermal history modelling of the H chondrite parent body. Astron. Astrophys. 545, A135.

Hevey, P.J., Sanders, I.S., 2006. A model for planetesimal meltdown by ^{26}Al and its implications for meteorite parent bodies. Meteorit. Planet. Sci. 41, 95–106.
Hille, M., Hu, Y., Huang, T.-Y., Teng, F.-Z., 2019. Homogeneous and heavy potassium isotopic composition of global oceans. Sci Bull 64, 1740–1742.
Holland, T.J.B., Powell, R., 2011. An improved and extended internally consistent thermodynamic dataset for phases of petrological interest, involving a new equation of state for solids. J. Metamorph. Geol. 29, 333–383.
Horwitz, E., Chiarizia, R., Dietz, M.L., 1992. A novel strontium-selective extraction chromatographic resin. Solvent Extr. Ion Exch. 10, 313–336.
Hu, Y., Chen, X.-Y., Xu, Y.-K., Teng, F.-Z., 2018. High-precision analysis of potassium isotopes by HR-MC-ICPMS. Chem. Geol. 493, 100–108.
Hu, X., Nan, X.-Y., Yu, H.-M., Huang, F., 2021a. High precision Rb isotope measurements by MC-ICP-MS. J. Anal. At. Spectrom. 36, 2744–2755.
Hu, X., Nan, X., Liu, X., Huang, F., 2022. Rubidium isotope compositions of the average upper continental crust and the Himalayan leucogranites: Implications for magmatic-fluid interaction. Geochim. Cosmochim. Acta 336, 165–176.
Hu, Y., Teng, F.-Z., Plank, T., Chauvel, C., 2020. Potassium isotopic heterogeneity in subducting oceanic plates. Sci. Adv. 6, eabb2472.
Hu, Y., Teng, F., Helz, R.T., Chauvel, C., 2021b. Potassium isotope fractionation during magmatic differentiation and the composition of the mantle. J. Geophys. Res. Solid Earth 126.
Hu, Y., Teng, F.-Z., Chauvel, C., 2021c. Potassium isotopic evidence for sedimentary input to the mantle source of Lesser Antilles lavas. Geochim. Cosmochim. Acta 295, 98–111.
Huang, T.-Y., Teng, F.-Z., Rudnick, R.L., Chen, X.-Y., Hu, Y., Liu, Y.-S., Wu, F.-Y., 2020. Heterogeneous potassium isotopic composition of the upper continental crust. Geochim. Cosmochim. Acta 278, 122–136.
Humayun, M., Clayton, R.N., 1995a. Potassium isotope cosmochemistry: Genetic implications of volatile element depletion. Geochim. Cosmochim. Acta 59, 2131–2148.
Humayun, M., Clayton, R.N., 1995b. Precise determination of the isotopic composition of potassium: Application to terrestrial rocks and lunar soils. Geochim. Cosmochim. Acta 59, 2115–2130.
Humayun, M., Koeberl, C., 2004. Potassium isotopic composition of Australasian tektites. Meteorit. Planet. Sci. 39, 1509–1516.
Huss, G.R., MacPherson, G.J., Wasserburg, G., Russell, S.S., Srinivasan, G., 2001. Aluminum-26 in calcium-aluminum-rich inclusions and chondrules from unequilibrated ordinary chondrites. Meteorit. Planet. Sci. 36, 975–997.
Jiang, Y., Koefoed, P., Pravdivtseva, O., Chen, H., Li, C.-H., Huang, F., Qin, L.-P., Liu, J., Wang, K., 2021. Early solar system aqueous activity: K isotope evidence from Allende. Meteorit. Planet. Sci. 56, 61–76.
Kimura, M., Ikeda, Y., 1998. Hydrous and anhydrous alterations of chondrules in Kaba and Mokoia CV chondrites. Meteorit. Planet. Sci. 33, 1139–1146.
Koefoed, P., Pravdivtseva, O., Chen, H., Gerritzen, C., Thiemens, M.M., Wang, K., 2020. Potassium isotope systematics of the LL4 chondrite Hamlet: Implications for chondrule formation and alteration. Meteorit. Planet. Sci. 55.
Ku, Y., Jacobsen, S.B., 2020. Potassium isotope anomalies in meteorites inherited from the protosolar molecular cloud. Sci. Adv. 6, eabd0511.
Kuhnel, W.W., Jacobsen, S.B., Li, Y., Ku, Y., Petaev, M.I., Huang, S., Wu, Z., Wang, K., 2021. High-temperature inter-mineral potassium isotope fractionation: implications for K-Ca–Ar chronology. ACS Earth Space Chem. 5, 2740–2754.
Larimer, J.W., Buseck, P.R., 1974. Equilibration temperatures in enstatite chondrites. Geochim. Cosmochim. Acta 38, 471–477.
LaTourrette, T., Wasserburg, G.J., 1998. Mg diffusion in anorthite: implications for the formation of early solar system planetesimals. Earth Planet. Sci. Lett. 158, 91–108.
Lewis, J.A., Jones, R.H., Brearley, A.J., 2022. Plagioclase alteration and equilibration in ordinary chondrites: Metasomatism during thermal metamorphism. Geochim. Cosmochim. Acta 316, 201–229.
Li, W., Cui, M., Pan, Q., Wang, J., Gao, B., Liu, S., Yuan, M., Su, B., Zhao, Y., Teng, F.-Z., 2022. High-precision potassium isotope analysis using the Nu Sapphire collision cell (CC)-MC-ICP-MS. Sci. China Earth Sci., 1–12.
Li, S., Li, W., Beard, B.L., Raymo, M.E., Wang, X., Chen, Y., Chen, J., 2019a. K isotopes as a tracer for continental weathering and geological K cycling. Proc. Natl. Acad. Sci. 116, 8740–8745.
Li, W., Liu, X.-M., Hu, Y., Teng, F.-Z., Hu, Y.-F., Chadwick, O.A., 2021a. Potassium isotopic fractionation in a humid and an arid soil–plant system in Hawai 'i. Geoderma 400, 115219.
Li, W., Liu, X.-M., Yan, H.u., Teng, F.-Z., Yongfeng, H.u., 2021b. Potassium isotopic fractionation during clay adsorption. Geochim. Cosmochim. Acta 304, 160–177.
Li, Y., Wang, W., Huang, S., Wang, K., Wu, Z., 2019b. First-principles investigation of the concentration effect on equilibrium fractionation of K isotopes in feldspars. Geochim. Cosmochim. Acta 245, 374–384.
Li, Y., Wang, W., Wu, Z., Huang, S., 2019c. First-principles investigation of equilibrium K isotope fractionation among K-bearing minerals. Geochim. Cosmochim. Acta 264, 30–42.
Liu, H., Wang, K., Sun, W.-D., Xiao, Y., Xue, Y.-Y., Tuller-Ross, B., 2020. Extremely light K in subducted low-T altered oceanic crust: Implications for K recycling in subduction zone. Geochim. Cosmochim. Acta 277, 206–223.
Liu, H., Xue, Y.-Y., Wang, K., Sun, W.-D., 2021a. Contributions of slab-derived fluids to ultrapotassic rocks indicated by K isotopes. Lithos 396, 106202.
Liu, H., Xue, Y.-Y., Zhang, G., Sun, W.-D., Tian, Z., Tuller-Ross, B., Wang, K., 2021b. Potassium isotopic composition of low-temperature altered oceanic crust and its impact on the global K cycle. Geochim. Cosmochim. Acta 311, 59–73.
Lodders, K., 2003. Solar system abundances and condensation temperatures of the elements. Astrophys. J. 591, 1220–1247.
Lodders, K., Fegley Jr, B., 1997. An oxygen isotope model for the composition of Mars. Icarus 126, 373–394.
Luck, J.-M., Othman, D.B., Albarède, F., 2005. Zn and Cu isotopic variations in chondrites and iron meteorites: Early solar nebula reservoirs and parent-body processes. Geochim. Cosmochim. Acta 69, 5351–5363.
Magna, T., Jiang, Y., Skála, R., Wang, K., Sossi, P.A., Žák, K., 2021. Potassium elemental and isotope constraints on the formation of tektites and element loss during impacts. Geochim. Cosmochim. Acta 312, 321–342.
Maurel, C., Bryson, J.F., Lyons, R.J., Ball, M.R., Chopdekar, R.V., Scholl, A., Ciesla, F.J., Bottke, W.F., Weiss, B.P., 2020. Meteorite evidence for partial differentiation and protracted accretion of planetesimals. Sci. Adv. 6, eaba1303.
McSween Jr, H.Y., Sears, D.W., Dodd, R.T., 1988. Thermal metamorphism. Meteor. Early Sol. Syst., 102–113.
Minster, J.F., Allégre, C.J., 1979. ^{87}Rb-^{87}Sr dating of L chondrites: effects of shock and brecciation. Meteoritics 14, 235–248.
Minster, J.-F., Ricard, L.-P., Allègre, C.J., 1979. ^{87}Rb-^{87}Sr chronology of enstatite meteorites. Earth Planet. Sci. Lett. 44, 420–440.
Miyamoto, M., Fujii, N., Takeda, H., 1982. Ordinary chondrite parent body-An internal heating model. In: In *Lunar and planetary science conference proceedIngs*, pp. 1145–1152.
Monnereau, M., Toplis, M.J., Baratoux, D., Guignard, J., 2013. Thermal history of the H-chondrite parent body: Implications for metamorphic grade and accretionary time-scales. Geochim. Cosmochim. Acta 119, 302–321.
Morgan, L.E., Ramos, D.P.S., Davidheiser-Kroll, B., Faithfull, J., Lloyd, N.S., Ellam, R.M., Higgins, J.A., 2018. High-precision 41K/39 K measurements by MC-ICP-MS indicate terrestrial variability of δ 41 K. J. Anal. At. Spectrom. 33, 175–186.
Moynier, F., Blichert-Toft, J., Telouk, P., Luck, J.-M., Albarède, F., 2007. Comparative stable isotope geochemistry of Ni, Cu, Zn, and Fe in chondrites and iron meteorites. Geochim. Cosmochim. Acta 71, 4365–4379.
Moynier, F., Paniello, R.C., Gounelle, M., Albarède, F., Beck, P., Podosek, F., Zanda, B., 2011. Nature of volatile depletion and genetic relationships in enstatite chondrites and aubrites inferred from Zn isotopes. Geochim. Cosmochim. Acta 75, 297–307.
Moynier, F., Hu, Y., Wang, K., Zhao, Y., Gérard, Y., Deng, Z., Moureau, J., Li, W., Simon, J.I., Teng, F.-Z., 2021. Potassium isotopic composition of various samples using a dual-path collision cell-capable multiple-collector inductively coupled plasma mass spectrometer. Nu instruments Sapphire. *Chem. Geol.* 571, 120144.
Nebel, O., Mezger, K., van Westrenen, W., 2011. Rubidium isotopes in primitive chondrites: Constraints on Earth's volatile element depletion and lead isotope evolution. Earth Planet. Sci. Lett. 305, 309–316.
Nie, N.X., Chen, X.-Y., Hopp, T., Hu, J.Y., Zhang, Z.J., Teng, F.-Z., Shahar, A., Dauphas, N., 2021a. Imprint of chondrule formation on the K and Rb isotopic compositions of carbonaceous meteorites. Sci. Adv. 7, eabl3929.
Nie, N.X., Dauphas, N., 2019. Vapor drainage in the protolunar disk as the cause for the depletion in volatile elements of the Moon. Astrophys. J. 884, L48.
Nie, N.X., Chen, X.-Y., Hopp, T., Hu, J., Zhang, Z., Teng, F.-Z., Shahar, A., Dauphas, N., 2021b. A condensation origin of potassium and rubidium isotopic variations in carbonaceous chondrites. LPI Contrib. 2609, 6217.
Nie, N.X., Dauphas, N., Hopp, T., Hu, J.Y., Zhang, Z.J., Yokochi, R., Ireland, T., Tissot, F. L., 2021c. Chromatography purification of Rb for accurate isotopic analysis by MC-ICPMS: A comparison between AMP-PAN, cation-exchange, and Sr resins. J. Anal. At. Spectrom..
Paniello, R.C., 2013. Volatization of extraterrestrial materials as determined by zinc isotopic analysis. Washington University in St, Louis. PhD thesis.
Paniello, R.C., Day, J.M.D., Moynier, F., 2012. Zinc isotopic evidence for the origin of the Moon. Nature 490, 376–379.
Parendo, C.A., Jacobsen, S.B., Wang, K., 2017. K isotopes as a tracer of seafloor hydrothermal alteration. Proc. Natl. Acad. Sci. 114, 1827–1831.
Pringle, E.A., Moynier, F., 2017. Rubidium isotopic composition of the Earth, meteorites, and the Moon: Evidence for the origin of volatile loss during planetary accretion. Earth Planet. Sci. Lett. 473, 62–70.
Qin, L., Dauphas, N., Wadhwa, M., Masarik, J., Janney, P.E., 2008. Rapid accretion and differentiation of iron meteorite parent bodies inferred from ^{182}Hf–^{182}W chronometry and thermal modeling. Earth Planet. Sci. Lett. 273, 94–104.
Ramos, D.P.S., Morgan, L.E., Lloyd, N.S., Higgins, J.A., 2018. Reverse weathering in marine sediments and the geochemical cycle of potassium in seawater: Insights from the K isotopic composition (41K/39K) of deep-sea pore-fluids. Geochim. Cosmochim. Acta 236, 99–120.
Richter, F.M., Davis, A.M., DePaolo, D.J., Watson, E.B., 2003. Isotope fractionation by chemical diffusion between molten basalt and rhyolite. Geochim. Cosmochim. Acta 67, 3905–3923.
Richter, F.M., Dauphas, N., Teng, F.-Z., 2009. Non-traditional fractionation of non-traditional isotopes: evaporation, chemical diffusion and Soret diffusion. Chem. Geol. 258, 92–103.
Richter, F.M., Mendybaev, R.A., Christensen, J.N., Ebel, D., Gaffney, A., 2011. Laboratory experiments bearing on the origin and evolution of olivine-rich chondrules. Meteorit. Planet. Sci. 46, 1152–1178.
Rubin, A.E., 2000. Petrologic, geochemical and experimental constraints on models of chondrule formation. Earth Sci. Rev. 50, 3–27.
Rubin, A.E., 2015. Impact features of enstatite-rich meteorites. Geochemistry 75, 1–28.
Rubin, A.E., Scott, E.R., Keil, K., 1997. Shock metamorphism of enstatite chondrites. Geochim. Cosmochim. Acta 61, 847–858.
Rudnick, R.L., Gao, S., 2003. 3.01 - Composition of the continental crust. In: Holland, H.D., Turekian, K.K. (Eds.), Treatise on Geochemistry. Pergamon, Oxford, pp. 1–64.

Russell, S.S., Srinivasan, G., Huss, G., Wasserburg, G., MacPherson, G., 1996. Evidence for widespread ^{26}Al in the solar nebula and constraints for nebula time scales. Science 273, 757–762.
Sanloup, C., Jambon, A., Gillet, P., 1999. A simple chondritic model of Mars. Phys. Earth Planet. Inter. 112, 43–54.
Savage, P.S., Moynier, F., Boyet, M., 2022. Zinc isotope anomalies in primitive meteorites identify the outer solar system as an important source of Earth's volatile inventory. Icarus 386, 115172.
Sears, D.W., Kallemeyn, G.W., Wasson, J.T., 1982. The compositional classification of chondrites: II The enstatite chondrite groups. Geochim. Cosmochim. Acta 46, 597–608.
Slater-Reynolds, V., McSween, H.Y., 2005. Peak metamorphic temperatures in type 6 ordinary chondrites: An evaluation of pyroxene and plagioclase geothermometry. Meteorit. Planet. Sci. 40, 745–754.
Sossi, P.A., Klemme, S., O'Neill, H., St, C., Berndt, J., Moynier, F., 2019. Evaporation of moderately volatile elements from silicate melts: experiments and theory. Geochim. Cosmochim. Acta 260, 204–231.
Steller, T., Burkhardt, C., Yang, C., Kleine, T., 2022. Nucleosynthetic zinc isotope anomalies reveal a dual origin of terrestrial volatiles. Icarus 386, 115171.
Stöffler, D., Keil, K., 1991. Shock metamorphism of ordinary chondrites. Geochim. Cosmochim. Acta 55, 3845–3867.
Sugiura, N., Arkani-Hamed, J., Strangway, D.W., 1986. Possible transport of carbon in meteorite parent bodies. Earth Planet. Sci. Lett. 78, 148–156.
Sugiura, N., Arkani-Hamed, J., Strangway, D., 1987. (1987) Possible transport of volatile trace elements in meteorite parent bodies. Memoirs of National Institute of Polar Research, Specical Issue 46, 216–225.
Sun, Y., Teng, F.-Z., Hu, Y., Chen, X.-Y., Pang, K.-N., 2020. Tracing subducted oceanic slabs in the mantle by using potassium isotopes. Geochim. Cosmochim. Acta 278, 353–360.
Tang, H., Dauphas, N., 2014. ^{60}Fe–^{60}Ni chronology of core formation in Mars. Earth Planet. Sci. Lett. 390, 264–274.
Taylor, S., Delaney, J., Ma, P., Herzog, G.F., Engrand, C., 2005. Isotopic fractionation of iron, potassium, and oxygen in stony cosmic spherules: Implications for heating histories and sources. Geochim. Cosmochim. Acta 69, 2647–2662.
Teng, F.-Z., McDonough, W.F., Rudnick, R.L., Walker, R.J., 2006. Diffusion-driven extreme lithium isotopic fractionation in country rocks of the Tin Mountain pegmatite. Earth Planet. Sci. Lett. 243, 701–710.
Teng, F.-Z., Dauphas, N., Watkins, J.M., 2017. Non-traditional stable isotopes: retrospective and prospective. Rev. Mineral. Geochem. 82, 1–26.
Tian, Z., Chen, H., Fegley, B., Lodders, K., Barrat, J.-A., Day, J.M.D., Wang, K., 2019. Potassium isotopic compositions of howardite-eucrite-diogenite meteorites. Geochim. Cosmochim. Acta 266, 611–632.
Tian, Z., Jolliff, B.L., Korotev, R.L., Fegley, B., Lodders, K., Day, J.M.D., Chen, H., Wang, K., 2020. Potassium isotopic composition of the Moon. Geochim. Cosmochim. Acta 280, 263–280.
Tian, Z., Magna, T., Day, J.M.D., Mezger, K., Scherer, E.E., Lodders, K., Hin, R.C., Koefoed, P., Bloom, H., Wang, K., 2021. Potassium isotope composition of Mars reveals a mechanism of planetary volatile retention. Proc. Natl. Acad. Sci. 118.
Tian, H.-C., Teng, F.-Z., Chen, X.-Y., Guo, Z.-X., Peng, X.-T., Yang, W., Xiao, Y.-L., 2022. Multi-mode chemical exchange in seafloor alteration revealed by lithium and potassium isotopes. Chem. Geol. 606, 121004.
Trieloff, M., Hopp, J., Gail, H.-P., 2022. Evolution of the parent body of enstatite (EL) chondrites. Icarus 373, 114762.
Tuller-Ross, B., Marty, B., Chen, H., Kelley, K.A., Lee, H., Wang, K., 2019. Potassium isotope systematics of oceanic basalts. Geochim. Cosmochim. Acta 259, 144–154.
Wang, K., Jacobsen, S.B., 2016a. Potassium isotopic evidence for a high-energy giant impact origin of the Moon. Nature 538, 487–490.
Wang, K., Jacobsen, S.B., 2016b. An estimate of the bulk silicate Earth potassium isotopic composition based on MC-ICPMS measurements of basalts. Geochim. Cosmochim. Acta 178, 223–232.
Wang, K., Li, W., Li, S., Tian, Z., Koefoed, P., Zheng, X.-Y., 2021a. Geochemistry and cosmochemistry of potassium stable isotopes. Geochemistry 81, 125786.
Wang, Z., Teng, F., Prelević, D., Liu, S., Zhao, Z., 2021b. Potassium isotope evidence for sediment recycling into the orogenic lithospheric mantle. Geochem. Perspect. Lett. 18, 43–47.
Wang, Z.-Z., Teng, F.-Z., Busigny, V., Liu, S.-A., 2022. Evidence from HP/UHP metasediments for recycling of isotopically heterogeneous potassium into the mantle. Am. Mineral. J. Earth Planet. Mater. 107, 350–356.
Wasson, J.T., Kallemeyn, G.W., 1988. Compositions of chondrites. Philos. Trans. R. Soc. Lond. Ser. Math. Phys. Sci. 325, 535–544.
Wedepohl, K.H., 1995. The composition of the continental crust. Geochim. Cosmochim. Acta 59, 1217–1232.
Weirich, J.R., Swindle, T.D., Isachsen, C.E., Sharp, T.G., Li, C., Downs, R.T., 2012. Source of potassium in shocked ordinary chondrites. Geochim. Cosmochim. Acta 98, 125–139.
Wlotzka, F., Palme, H., Spettel, B., Wänke, H., Fredriksson, K., Noonan, A.F., 1983. Alkali differentiation in LL-chondrites. Geochim. Cosmochim. Acta 47, 743–757.
Wombacher, F., Rehkämper, M., Mezger, K., Bischoff, A., Münker, C., 2008. Cadmium stable isotope cosmochemistry. Geochim. Cosmochim. Acta 72, 646–667.
Wood, B.J., Banno, S., 1973. Garnet-orthopyroxene and orthopyroxene-clinopyroxene relationships in simple and complex systems. Contrib. Mineral. Petrol. 42, 109–124.
Wood, B.J., Smythe, D.J., Harrison, T., 2019. The condensation temperatures of the elements: A reappraisal. Am. Mineral. 104, 844–856.
Xu, Y.-K., Hu, Y., Chen, X.-Y., Huang, T.-Y., Sletten, R.S., Zhu, D., Teng, F.-Z., 2019. Potassium isotopic compositions of international geological reference materials. Chem. Geol. 513, 101–107.
Yokoyama, T., Misawa, K., Okano, O., Shih, C.-Y., Nyquist, L.E., Simon, J.I., Tappa, M.J., Yoneda, S., 2017. Extreme early solar system chemical fractionation recorded by alkali-rich clasts contained in ordinary chondrite breccias. Earth Planet. Sci. Lett. 458, 233–240.
Yoshizaki, T., McDonough, W.F., 2020. The composition of Mars. Geochim. Cosmochim. Acta 273, 137–162.
Yu Y., Hewins R. H., Alexander C. M. O.'D. and Wang J. 2003. Experimental study of evaporation and isotopic mass fractionation of potassium in silicate melts. Geochim. Cosmochim. Acta 67, 773–786.
Zeng, H., Rozsa, V.F., Nie, N.X., Zhang, Z., Pham, T.A., Galli, G., Dauphas, N., 2019. Ab initio calculation of equilibrium isotopic fractionations of potassium and rubidium in minerals and water. ACS Earth Space Chem. 3, 2601–2612.
Zhang, Y., 2010. Diffusion in minerals and melts: theoretical background. Rev. Mineral. Geochem. 72, 5–59.
Zhang, Z., Ma, J., Zhang, L., Liu, Y., Wei, G., 2018. Rubidium purification via a single chemical column and its isotope measurement on geological standard materials by MC-ICP-MS. J. Anal. At. Spectrom. 33, 322–328.
Zhang, Z.J., Nie, N.X., Mendybaev, R.A., Liu, M.-C., Hu, J.J., Hopp, T., Alp, E.E., Lavina, B., Bullock, E.S., McKeegan, K.D., 2021. Loss and isotopic fractionation of alkali elements during diffusion-limited evaporation from molten silicate: Theory and experiments. ACS Earth Space Chem..
Zhao, C., Lodders, K., Bloom, H., Chen, H., Tian, Z., Koefoed, P., Pető, M.K., Wang, K., 2020. Potassium isotopic compositions of enstatite meteorites. Meteorit. Planet. Sci. 55, 1404–1417.